

Towards HPC simulations of Billion-cell Reservoirs by Multiscale Mixed Methods

Alfredo Jaramillo^{a,*}, Rafael T. Guiraldello^a, Stevens Paz^a, Roberto F. Ausas^a,
Fabricio S. Sousa^a, Felipe Pereira^b, Gustavo C. Buscaglia^a

(a) Instituto de Ciências Matemáticas e de Computação, Universidade de São Paulo

(b) Department of Mathematical Sciences, The University of Texas at Dallas

March 16, 2021

Abstract

A three dimensional parallel implementation of Multiscale Mixed Methods based on non-overlapping domain decomposition techniques is proposed for multi-core computers and its computational performance is assessed by means of numerical experimentation. As a prototypical method, from which many others can be derived, the Multiscale Robin Coupled Method is chosen and its implementation explained in detail. Numerical results for problems ranging from millions up to more than 2 billion computational cells in highly heterogeneous anisotropic rock formations based on the SPE10 benchmark are shown. The proposed implementation relies on direct solvers for both local problems and the interface coupling system. We find good weak and strong scalability as compared against a state-of-the-art global fine grid solver based on Algebraic Multigrid preconditioning in single and two-phase flow problems.

Keywords: Porous media, Darcy's law, Two-phase flow, High Performance Computing, Multi-scale method, Domain Decomposition.

1 Introduction

Reservoir simulation is a challenging problem that demands intensive use of computational resources. For very thick reservoirs, as is the case in the Brazilian pre-salt layer, discrete models require a number of computational cells in the order of billions so as to achieve results with the required level of accuracy. Numerical methods based on a single global scale discretization along with preconditioned Krylov iterative strategies to solve the resulting system of equations may fail to handle such extreme levels of discretization efficiently.

In the last decade, multilevel and multiscale methodologies based on domain decomposition have provided an alternative with potential to deliver reasonably accurate results [1, 2, 3] with good scalability properties. Multiscale methods decompose the global fine-scale problem into several local problems, whose solutions are called *Multiscale Basis Functions* (MBFs) and are computed by setting suitable boundary conditions on the local domains. The MBFs computations are independent from each other and therefore its parallelization is straightforward in multi-core computers. On the interface between the local domains the compatibility conditions, namely, pressure and/or flux continuity, are imposed weakly on a coarser scale related to that of the domain decomposition. The resulting relaxed interface problem is solved using the computed MBFs and its coarse-grid interface solution is used to locally reconstruct the multiscale solution. Multiscale methods based on domain decomposition techniques aiming at the accurate approximation of velocity and pressure fields have been the focus of intensive research over the last years [4, 5, 6, 7, 8, 9, 10]. However, in the context of reservoir simulation involving highly anisotropic rock formations exhibiting regions with multiple channels and obstacles, the accuracy of the multiscale methods can seriously deteriorate [11, 12]. Also, a lack of High Performance Computing reports involving high-resolution problems (in the order of one billion cells) can be identified in the literature where most of the reported results are only two dimensional and/or involve small/middle size problems [13, 14, 15]. The behavior in terms of accuracy and scalability of such methods in large scale complex three dimensional

*Alfredo Jaramillo. ajaramillopalma@gmail.com. Institute of Mathematics and Computer Science of the University of São Paulo. Av. Trab. São Carlsense, 400 - Centro, São Carlos - SP, Brazil, 13566-590.

formations, which are the target problems these methods have originally been devised to, is still an area of active research [16].

We focus our analysis on the Multiscale Robin Coupled Method (MRCM) [5], a recently proposed method that generalizes the Multiscale Mixed Method (MuMM) [4]. The compatibility conditions on the interface are enforced by means of a Robin type boundary condition which depends on an algorithmic parameter that can be adjusted locally or globally, leading to a family of methods of which the Multiscale Mortar Mixed Finite Element Method [6] and the Multiscale Hybrid-Mixed Finite Element Method [10] are particular cases. This feature of the method is attractive, since it provides a general framework that can be useful to study the accuracy and performance of multiscale mixed methods based on non-overlapping domain decomposition.

Several aspects of this method have been explored in the last few years. For instance, the choice of the MRCM algorithmic parameter has in part been surveyed in [5]. Also, Rocha et al [12] have proposed an adaptive strategy to improve accuracy by setting this algorithmic parameter as a function of the permeability contrast. Concerning the interface spaces for the flux and pressure coupling unknowns on the skeleton of the domain decomposition, Guiraldello et al [17] and Rocha et al [18, 19] have introduced, respectively, informed and physically based basis functions that can yield more accurate results than polynomial spaces. Finally, the coupling to a transport solver in the linear passive case [20] and in the non-linear (two phase flow) case [12] have also been carefully investigated.

The aforementioned contributions illustrate the potential of multiscale mixed approximations for the flow calculations in high-contrast permeability fields. However, in this papers the authors assess the method by looking at accuracy and convergence to fine grid solutions in two dimensional setting involving no more than $\sim 10^4$ unknowns, the three dimensional case being left aside. In this work we fill in this gap by showing high-resolution three dimensional numerical results produced by a HPC implementation of the MRCM. Weak and strong scalability as well as accuracy of the method are investigated by comparison to fine grid solutions. These solutions are based on a classical finite volume discretization scheme considering sizes ranging from ~ 20 million to a few billion computational cells, defined by suitably refining the challenging SPE10 industry benchmark [21].

The structure of this paper is as follows: Section 2 provides the mathematical models and numerical techniques used in this work, which involves a global elliptic solver (the Fine Grid method) and a three-dimensional implementation of the MRCM. Details on several implementation aspects are provided. Computational times and efficiency are reported in Section 3 for both elliptic solvers. Special attention is given to the weak and strong scalability and the gain factor obtained in solving problems by a multiscale method. To assess the precision of the multiscale solution two-phase flow simulations are also performed within an IMPES [22, 23, 24, 25] approximation and the results for each one of the solvers are compared. Finally, some concluding remarks are drawn in Section 4.

2 Mathematical model and numerical schemes

Consider a domain $\Omega \subset \mathbb{R}^3$ and two-phase flow of water and oil with respective saturations fields denoted by S_w and S_o , that depend both on position \mathbf{x} and time t . Capillary pressure and gravity effects are neglected. Assuming saturated porous media we have the restriction

$$S_w + S_o = 1. \quad (2.1)$$

The evolution of S_w is modeled by the Buckley-Leverett equation

$$\frac{\partial S_w}{\partial t} + \nabla \cdot (\varphi(S_w)\mathbf{u}) = 0, \quad (2.2)$$

where φ is the so called fractional flow function. By rescaling the time variable the porosity of the medium, which is assumed constant in this work, is removed from eq. (2.2).

Velocity \mathbf{u} and pressure field p satisfy the Darcy's law and the continuity equation with prescribed boundary conditions

$$\mathbf{u} = -\lambda(S_w)\mathbf{K} \nabla p \quad \text{in } \Omega \quad (2.3)$$

$$\nabla \cdot \mathbf{u} = f \quad \text{in } \Omega \quad (2.4)$$

$$p = g_p \quad \text{on } \partial\Omega_p \quad (2.5)$$

$$\mathbf{u} \cdot \hat{\mathbf{n}} = g_u \quad \text{on } \partial\Omega_u \quad (2.6)$$

where \mathbf{K} is the permeability tensor assumed to be diagonal and anisotropic, i.e., $\mathbf{K} = \text{diag}(K^{11}, K^{22}, K^{33})$, λ is the total mobility function, g_p , g_u and f are given *forcing* data. The functions φ and λ read

$$\lambda(S_w) = \frac{S_w^2}{\mu_w} + \frac{(1 - S_w)^2}{\mu_o} \quad \text{and} \quad \varphi(S_w) = \frac{(\mu_o/\mu_w)S_w^2}{(\mu_o/\mu_w)S_w^2 + (1 - S_w)^2}.$$

in which μ_w and μ_o stands for the viscosity of the water and oil phases, respectively.

2.1 Domain decomposition and Darcy solvers

The domain is decomposed into non-overlapping subdomains Ω^ℓ of typical size H , such that $\Omega = \bigcup_\ell \Omega^\ell$. The skeleton of the domain decomposition is denoted by $\Gamma = \bigcup_\ell \Gamma_{\ell, \ell'}$, with $\Gamma_{\ell, \ell'} = \bar{\Omega}^\ell \cap \bar{\Omega}^{\ell'}$. Let us denote $\hat{\mathbf{n}}^\ell$ a unit vector normal to Ω^ℓ , define $\hat{\mathbf{n}} = \hat{\mathbf{n}}^{\min\{\ell, \ell'\}}$ and use $+$ and $-$ superscripts to refer to the two-sided limits approaching Γ .

Two different Darcy solvers are implemented to approximate the solution to (2.3)-(2.6), namely, a fine grid global method and the MRCM. The main difference between these two solvers is that continuity of the unknown fields \mathbf{u} and p on the skeleton of the domain decomposition is relaxed in the MRCM by imposing

$$\int_\Gamma (\mathbf{u}^+ - \mathbf{u}^-) \cdot \hat{\mathbf{n}} v_H d\Gamma = 0, \quad \forall v_H \in \mathcal{P}_H, \quad (2.7)$$

$$\int_\Gamma (p^+ - p^-) w_H d\Gamma = 0, \quad \forall w_H \in \mathcal{U}_H, \quad (2.8)$$

where \mathcal{P}_H and \mathcal{U}_H , are suitably defined spaces over the skeleton Γ such that mass conservation is satisfied at a coarse scale \bar{H} . By setting $\mathcal{P}_H = \mathcal{P}_h$ and $\mathcal{U}_H = \mathcal{U}_h$ the solutions of both methods coincide.

A key ingredient for both solvers is a Finite Volume discretization method that, for completeness, is recalled next. For any subdomain $\omega \subset \Omega$, we consider a hexahedral mesh to discretize (2.4) by considering (2.3) along two-point formulas for the fluxes as in [5]. Consider computational cells of sizes h_{x_1} , h_{x_2} , h_{x_3} in each direction, $h = \max\{h_{x_1}, h_{x_2}, h_{x_3}\}$ denotes the maximum of h_{x_j} and the total number of cells is denoted by N^ω . The product of λ and \mathbf{K} in Darcy's law (2.3) is referred to as $\tilde{\mathbf{K}}$. With this, one ends up with the system of equations

$$\begin{cases} -a_{i-1,j,k} p_{i-1,j,k} - a_{i,j,k} p_{i+1,j,k} - b_{i,j-1,k} p_{i,j-1,k} - b_{i,j,k} p_{i,j+1,k} \\ -c_{i,j,k-1} p_{i,j,k-1} - c_{i,j,k} p_{i,j,k+1} + d_{i,j,k} p_{i,j,k} = f_{i,j,k}, \end{cases} \quad (2.9)$$

where

$$\begin{cases} a_{i,j,k} = \frac{\tilde{K}_{i+\frac{1}{2},j,k}^{11}}{h_{x_1}^2}, \quad b_{i,j,k} = \frac{\tilde{K}_{i,j+\frac{1}{2},k}^{22}}{h_{x_2}^2}, \quad c_{i,j,k} = \frac{\tilde{K}_{i,j,k+\frac{1}{2}}^{33}}{h_{x_3}^2}, \\ d_{i,j,k} = \frac{\tilde{K}_{i+\frac{1}{2},j,k}^{11}}{h_{x_1}^2} + \frac{\tilde{K}_{i-\frac{1}{2},j,k}^{11}}{h_{x_1}^2} + \frac{\tilde{K}_{i,j+\frac{1}{2},k}^{22}}{h_{x_2}^2} + \frac{\tilde{K}_{i,j-\frac{1}{2},k}^{22}}{h_{x_2}^2} + \frac{\tilde{K}_{i,j,k+\frac{1}{2}}^{33}}{h_{x_3}^2} + \frac{\tilde{K}_{i,j,k-\frac{1}{2}}^{33}}{h_{x_3}^2}, \\ \tilde{K}_{i\pm\frac{1}{2},j,k}^{11} = \frac{2 \hat{K}_{i,j,k}^{11} \hat{K}_{i\pm 1,j,k}^{11}}{\hat{K}_{i,j,k}^{11} + \hat{K}_{i\pm 1,j,k}^{11}}, \quad \tilde{K}_{i,j\pm\frac{1}{2},k}^{22} = \frac{2 \hat{K}_{i,j,k}^{22} \hat{K}_{i,j\pm 1,k}^{22}}{\hat{K}_{i,j,k}^{22} + \hat{K}_{i,j\pm 1,k}^{22}}, \quad \tilde{K}_{i,j,k\pm\frac{1}{2}}^{33} = \frac{2 \hat{K}_{i,j,k}^{33} \hat{K}_{i,j,k\pm 1}^{33}}{\hat{K}_{i,j,k}^{33} + \hat{K}_{i,j,k\pm 1}^{33}}, \end{cases} \quad (2.10)$$

and i, j, k the cells indices along the x_1 , x_2 and x_3 axis. Also, in (2.10), $\tilde{K}_{i,j,k}^{ll}$ terms correspond to the so called harmonic mean of the permeability diagonal entries of \hat{K} . To account for the boundary conditions some of these terms for cells having a face on the boundary $\partial\Omega$ must be modified (see [5]).

2.1.1 The global fine grid solver

Assembling eqs. (2.9)-(2.10) for the case $\omega = \Omega$ leads to a linear system given by

$$\mathcal{A}^h \mathbf{p}^h = \mathbf{f}^h, \quad (2.11)$$

where $\mathcal{A}^h \in \mathbb{R}^{N^\Omega \times N^\Omega}$ represents a sparse matrix operator and $\mathbf{p}^h \in \mathbb{R}^{N^\Omega}$ is the global vector of cell pressure unknowns whit N^Ω standing for the total number of cells in the global (target) problem. Once this discrete pressure field is found the discrete velocity field \mathbf{u}^h can be recovered at the cell faces by means of two-point formulas, e.g.,

$$u_{i+\frac{1}{2},j,k} = -\tilde{K}_{i+\frac{1}{2},j,k}^{11} \frac{p_{i+1,j,k} - p_{i,j,k}}{h_{x_1}}, \quad (2.12)$$

with analogous definitions for other cell fluxes. Typical sizes of the global systems to be solved in this work varies between a few million up to a few billion cells, that precludes the use of direct solvers.

2.1.2 A domain decomposition Multiscale Mixed method

In this section we recall the basic ingredients of the multiscale method adopted in this work, the MRCM, that has been presented in detail in [5, 17]. This multiscale strategy localizes the problem (2.3)-(2.6) into each subdomain Ω^ℓ . The boundary conditions (2.5)-(2.6) are imposed at the regions of $\partial\Omega^\ell$ that lay on $\partial\Omega$. To fully define the local problems, Robin boundary conditions are imposed at the regions of $\partial\Omega^\ell$ that intercept Γ . One arrives to a multiscale solution in Ω by coupling the local solutions through the weak compatibility conditions (2.7) and (2.8). The differential formulation of this method reads: Find subdomain solutions $(\mathbf{u}^\ell, p^\ell)$, decomposed as $\mathbf{u}^\ell = \hat{\mathbf{u}}^\ell + \bar{\mathbf{u}}^\ell$, $p^\ell = \hat{p}^\ell + \bar{p}^\ell$ and interface fields (U_H, P_H) satisfying:

$$\left. \begin{aligned} \bar{\mathbf{u}}^\ell &= -\mathbf{K} \nabla \bar{p}^\ell && \text{in } \Omega^\ell \\ \nabla \cdot \bar{\mathbf{u}}^\ell &= f && \text{in } \Omega^\ell \\ \bar{p}^\ell &= g_p && \text{on } \partial\Omega^\ell \cap \partial\Omega_p \\ \bar{\mathbf{u}}^\ell \cdot \hat{\mathbf{n}}^\ell &= g_u && \text{on } \partial\Omega^\ell \cap \partial\Omega_u \\ -\beta^\ell \bar{\mathbf{u}}^\ell \cdot \hat{\mathbf{n}}^\ell + \bar{p}^\ell &= 0 && \text{on } \partial\Omega^\ell \cap \Gamma \end{aligned} \right\} \quad (2.13)$$

$$\left. \begin{aligned} \hat{\mathbf{u}}^\ell &= -\mathbf{K} \nabla p^\ell && \text{in } \Omega^\ell \\ \nabla \cdot \hat{\mathbf{u}}^\ell &= 0 && \text{in } \Omega^\ell \\ \hat{p}^\ell &= 0 && \text{on } \partial\Omega^\ell \cap \partial\Omega_p \\ \hat{\mathbf{u}}^\ell \cdot \hat{\mathbf{n}}^\ell &= 0 && \text{on } \partial\Omega^\ell \cap \partial\Omega_u \\ -\beta^\ell \hat{\mathbf{u}}^\ell \cdot \hat{\mathbf{n}}^\ell + \hat{p}^\ell &= -\beta^\ell U_H \hat{\mathbf{n}} \cdot \hat{\mathbf{n}}^\ell + P_H && \text{on } \partial\Omega^\ell \cap \Gamma \end{aligned} \right\} \quad (2.14)$$

$$\sum_\ell \int_{\partial\Omega^\ell \cap \Gamma} (\mathbf{u}^\ell \cdot \hat{\mathbf{n}}^\ell) \phi d\Gamma = 0 \quad \forall \phi \in \mathcal{P}_H \quad (2.15)$$

$$\sum_\ell \int_{\partial\Omega^\ell \cap \Gamma} \beta^\ell (\mathbf{u}^\ell \cdot \hat{\mathbf{n}}^\ell - U_H \hat{\mathbf{n}} \cdot \hat{\mathbf{n}}^\ell) \hat{\mathbf{n}}^\ell \cdot \hat{\mathbf{n}} \phi d\Gamma = 0 \quad \forall \phi \in \mathcal{U}_H \quad (2.16)$$

where β^ℓ are the Robin condition parameters. The differential problems (2.13) and (2.14) are solved independently. In addition an interface linear problem that results from (2.15)-(2.16) must be solved. The interface problem can be written by first introducing a finite dimensional space $\mathcal{V}_H = \text{span}\{\phi_1, \dots, \phi_{N_V}\}$ defined on the skeleton of the domain decomposition such that the interface fields read

$$P_H = \sum_{k=1}^{N_V} \pi_k^p \phi_k, \quad U_H = \sum_{k=1}^{N_V} \pi_k^u \phi_k. \quad (2.17)$$

Remark 1. Although the MRCM allows for the use different spaces for P_H and U_H [5], in this work, for simplicity, we restrict ourselves to the case where both spaces are the same. Several choices of interface spaces have been proposed in [5, 17, 18].

By denoting $X = (\pi_1^p, \dots, \pi_{N_V}^p, \pi_1^u, \dots, \pi_{N_V}^u)^\top$ allows us to write the conditions (2.15)-(2.16) as the linear system

$$\mathcal{A}^{\text{int}} X = \mathbf{b}^{\text{int}} \rightarrow \begin{bmatrix} A^{PP} & A^{PU} \\ A^{UP} & A^{UU} \end{bmatrix} \begin{bmatrix} \pi^p \\ \pi^u \end{bmatrix} = \begin{bmatrix} b^P \\ b^U \end{bmatrix}, \quad (2.18)$$

where

$$A_{ij}^{PP} = \sum_{\substack{\ell, \ell' \\ \ell < \ell'}} \int_{\Gamma_{\ell, \ell'}} \{\hat{\mathbf{u}}_h(\phi_j, 0)\} \phi_i d\Gamma, \quad A_{ij}^{PU} = \sum_{\substack{\ell, \ell' \\ \ell < \ell'}} \int_{\Gamma_{\ell, \ell'}} \{\hat{\mathbf{u}}_h(0, \phi_j)\} \phi_i d\Gamma, \quad b_i^P = \sum_{\substack{\ell, \ell' \\ \ell < \ell'}} \int_{\Gamma_{\ell, \ell'}} \{\bar{\mathbf{u}}_h\} \phi_i d\Gamma. \quad (2.19)$$

In (2.19) $\hat{\mathbf{u}}_h^\ell(\phi_j, 0)$ and $\hat{\mathbf{u}}_h^\ell(0, \phi_j)$ is the velocity part of the so called Multiscale Basis Functions (MBFs) (see [5]) obtained as solutions to subdomain problem (2.14) by taking $(P_H, U_H) = (\phi_j, 0)$ and $(P_H, U_H) = (0, \phi_j)$, respectively. Similarly, $\hat{p}_h^\ell(\phi_j, 0)$ and $\hat{p}_h^\ell(0, \phi_j)$ denotes the corresponding pressure part of these local problems. Also, $\bar{\mathbf{u}}_h^\ell$ are the particular solutions of the local problems (2.13). In (2.19), $\{\cdot\}$ stands for the jump operator of a vector field \mathbf{v} on Γ , i.e., $\{\mathbf{v}\} = (\mathbf{v}^\ell - \mathbf{v}^{\ell'}) \cdot \hat{\mathbf{n}}$ at each $\Gamma_{\ell, \ell'}$. For the second row block of (2.18) one has:

$$A_{ij}^{UP} = \sum_{\substack{\ell, \ell' \\ \ell < \ell'}} \int_{\Gamma_{\ell, \ell'}} (\beta_i \hat{\mathbf{u}}_h^\ell(\phi_j, 0) + \beta_j \hat{\mathbf{u}}_h^\ell(\phi_j, 0)) \cdot \hat{\mathbf{n}} \phi_i d\Gamma, \quad (2.20)$$

$$A_{ij}^{UU} = \sum_{\substack{\ell, \ell' \\ \ell < \ell'}} \int_{\Gamma_{\ell, \ell'}} \left[(\beta_\ell \hat{\mathbf{u}}_h^\ell(0, \phi_j) + \beta_{\ell'} \hat{\mathbf{u}}_h^{\ell'}(0, \phi_j)) \cdot \hat{\mathbf{n}} - (\beta_\ell + \beta_{\ell'}) \phi_j \right] \phi_i d\Gamma \quad (2.21)$$

$$b_i^U = - \sum_{\substack{\ell, \ell' \\ \ell < \ell'}} \int_{\Gamma_{\ell, \ell'}} [\beta_\ell \bar{\mathbf{u}}_h^\ell + \beta_{\ell'} \bar{\mathbf{u}}_h^{\ell'}] \cdot \hat{\mathbf{n}} \phi_i d\Gamma \quad (2.22)$$

Once P_H and U_H are obtained by solving (2.18), the multiscale solution is locally recovered by means of (2.14). Notice that one has two options to perform this last step. The first one is just computing the combinations

$$p^\ell = \sum_{k=1}^{N_\nu} [\pi_k^p \hat{p}_h^\ell(\phi_k, 0) + \pi_k^u \hat{p}_h^\ell(0, \phi_k)] + \bar{p}_h, \quad \mathbf{u}^\ell = \sum_{k=1}^{N_\nu} [\pi_k^p \hat{\mathbf{u}}_h^\ell(\phi_k, 0) + \pi_k^u \hat{\mathbf{u}}_h^\ell(0, \phi_k)] + \bar{\mathbf{u}}_h, \quad (2.23)$$

if the information is still available in memory. Otherwise, we can use (2.17) and explicitly solve problems (2.13) and (2.14).

We still need to define the space \mathcal{V}_H . To do so, let H_{x_i} ($i = 1, 2, 3$) be the length of the subdomains Ω^ℓ (integer multiple of the cells length h_{x_i}) along some direction and \bar{H}_{x_i} be a multiple of h_{x_i} such that $h_{x_i} \leq \bar{H}_{x_i} \leq H_{x_i}$, $i = 1, 2, 3$. One introduces first the fine grid space \mathcal{V}_h on Γ . To that end, consider some arbitrary interface $\Gamma_{\ell, \ell'}$, as shown in Figure 1 a) and b), the intersection of the volumetric cells with $\Gamma_{\ell, \ell'}$ induces a decomposition of $\Gamma_{\ell, \ell'}$ into rectangles of lengths h_{x_i} , h_{x_j} for some $i, j \in \{1, 2, 3\}$. The space \mathcal{V}_H corresponds to a coarsening of \mathcal{V}_h obtained by condensing degrees of freedom as shown in Fig. 1 c). A basis for \mathcal{V}_H can be obtained by selecting the functions defined on Γ that assume the value 1 at some of these condensate regions (the yellow portion in Fig. 1) and 0 on the rest of Γ . This basis parameterized by \bar{H}_{x_i} , $i = 1 \dots 3$, is denoted hereafter by $\{\phi_k\}$ and its cardinal is equal to

$$\#\{\phi_j\} = \underbrace{(N_{d_1} - 1)N_{d_2}N_{d_3}}_{\text{\#interfaces}} \underbrace{\frac{H_{x_2}}{\bar{H}_{x_2}} \frac{H_{x_3}}{\bar{H}_{x_3}}}_{\text{dof per interface}} + (N_{d_2} - 1)N_{d_1}N_{d_3} \frac{H_{x_1}}{\bar{H}_{x_1}} \frac{H_{x_3}}{\bar{H}_{x_3}} + (N_{d_3} - 1)N_{d_1}N_{d_2} \frac{H_{x_1}}{\bar{H}_{x_1}} \frac{H_{x_2}}{\bar{H}_{x_2}}. \quad (2.24)$$

where $N_{d_i} = 1/H_{x_i}$, $i = 1, 2, 3$. An example of the condensation of degrees of freedom on Γ is illustrated in Fig. 1 where $\bar{H}_{x_1} = 2h_{x_1}$ and $\bar{H}_{x_2} = 3h_{x_2}$. There, six degrees of freedom from the fine grid, as shown in Fig. 1 b), are condensate into a single one, as displayed in Fig. 1 c).

Next, fix a subdomain Ω^ℓ . Let us denote by \mathcal{I}^ℓ the indices of the functions ϕ_k with support contained in $\partial\Omega^\ell$, i.e., $\mathcal{I}^\ell = \{k \in \mathbb{N} : \text{supp}(\phi_k) \subset \partial\Omega^\ell \cap \Gamma \neq \emptyset\}$. The MBFs are computed by means of a discretization analogous to that used for the fine grid solution, in this case subject to Robin boundary conditions. Denoting by $\hat{\mathbf{p}}_{\ell, k; P}$ the column vector of cell pressure values corresponding to $\hat{\mathbf{p}}_h^\ell(\phi_k, 0)$ and by $\hat{\mathbf{p}}_{\ell, k; U}$ the corresponding one for $\hat{\mathbf{p}}_h^\ell(0, \phi_k)$, the following local (fine grid) systems must be solved

$$\mathcal{A}_\ell^H \hat{\mathbf{p}}_{\ell, k; P} = \mathbf{f}_{\ell, k; P}^H, \quad \mathcal{A}_\ell^H \hat{\mathbf{p}}_{\ell, k; U} = \mathbf{f}_{\ell, k; U}^H \quad \text{for } k \in \mathcal{I}^\ell. \quad (2.25)$$

Abbreviating by $\gamma = (g_p, g_u, f)$ the forcing data and denoting by $\bar{\mathbf{p}}_{\ell; \gamma}$ the discrete solution of the particular problem (2.13) and by $\mathbf{f}_{\ell; \gamma}^H$ its right hand side, this problem is written as

$$\mathcal{A}_\ell^H \bar{\mathbf{p}}_{\ell; \gamma} = \mathbf{f}_{\ell; \gamma}^H. \quad (2.26)$$

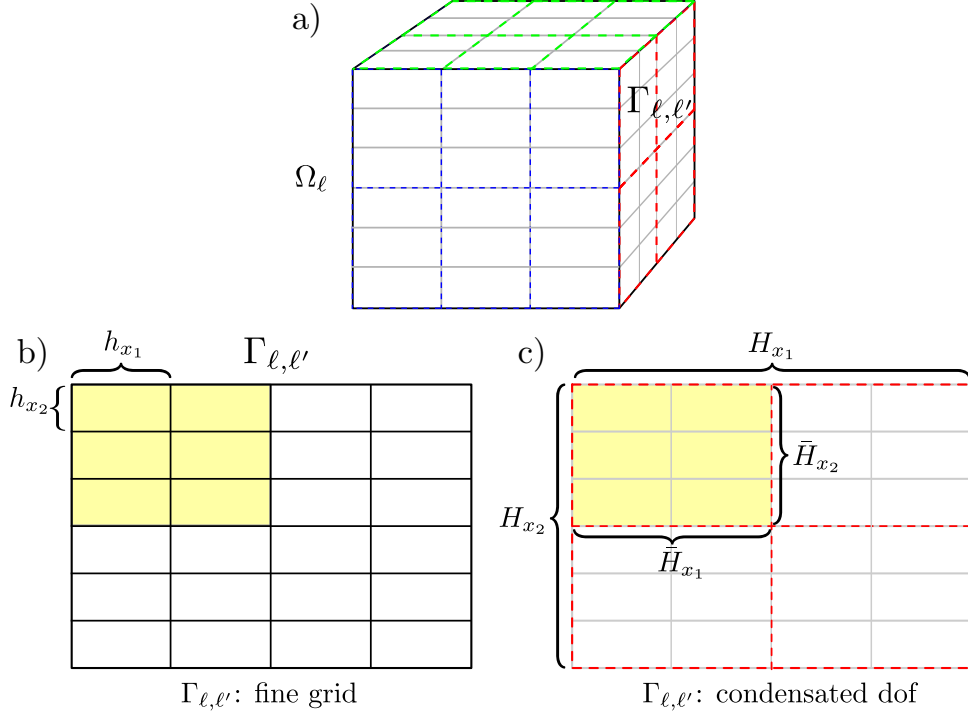


Figure 1: Example showing the condensate degrees of freedom at the interfaces between subdomains. In this particular case the number of degrees of freedom is decreased by a factor of $\frac{\bar{H}_{x_1}}{h_{x_1}} \frac{\bar{H}_{x_2}}{h_{x_2}} = 2 \cdot 3 = 6$.

Now, for a subdomain totally immersed in Ω (i.e., $\Omega^\ell \cap \partial\Omega = \emptyset$) the number of linear problems written in (2.25) corresponds to

$$2 \cdot |\mathcal{I}^\ell| = 2 \cdot \left(\overbrace{2 \frac{H_{x_2}}{\bar{H}_{x_2}} \frac{H_{x_3}}{\bar{H}_{x_3}}}^{\text{dof interfaces } || \text{ to } x_2-x_3} + \overbrace{2 \frac{H_{x_1}}{\bar{H}_{x_1}} \frac{H_{x_3}}{\bar{H}_{x_3}}}^{\text{dof interfaces } || \text{ to } x_1-x_3} + \overbrace{2 \frac{H_{x_1}}{\bar{H}_{x_1}} \frac{H_{x_2}}{\bar{H}_{x_2}}}^{\text{dof interfaces } || \text{ to } x_1-x_2} \right),$$

in cases where each H_{x_i} is equal to a constant H and each \bar{H}_{x_i} is equal to a constant \bar{H} , one has that $2 \cdot |\mathcal{I}^\ell| = 12 H/\bar{H}$. Therefore, for most of the situations considered in this work, where $\bar{H} = H$, we need to solve 12 linear problems to construct the multiscale basis functions $\hat{\mathbf{p}}_{\ell,k;P}$ and $\hat{\mathbf{p}}_{\ell,k;U}$ for each interior subdomain Ω^ℓ . Typical sizes of these local problems involve a few thousand unknowns that suggest that the use of direct solvers might be a computationally effective choice.

2.2 The fine grid transport solver

The classical Implicit Pressure Explicit Saturation (IMPES) method was used to perform two-phase flow simulations. In such methodology, one computes first the velocity field \mathbf{u} by calling a Darcy solver (here, Fine Grid or MRCM) and then updates the saturation field \mathbf{S} . These two steps are repeated sequentially. For the saturation step, equation (2.2) is discretized by means of a Finite Volume Method, where the computational cells have sizes h_{x_1} , h_{x_2} and h_{x_3} on each axis. Thus, knowing the discrete field \mathbf{S}^n at time t^n , the update $\mathbf{S}^{n+1} = \mathbf{S}(t^n + \Delta t_s)$ is computed according to:

$$\begin{aligned} \mathbf{S}_{i,j,k}^{n+1} = & \mathbf{S}_{i,j,k}^n + \frac{\Delta t_s}{h_{x_1}} \left(\varphi_{i+\frac{1}{2},j,k} u_{i+\frac{1}{2},j,k}^n + \varphi_{i-\frac{1}{2},j,k} u_{i-\frac{1}{2},j,k}^n \right) \\ & + \frac{\Delta t_s}{h_{x_2}} \left(\varphi_{i,j+\frac{1}{2},k} u_{i,j+\frac{1}{2},k}^n + \varphi_{i,j-\frac{1}{2},k} u_{i,j-\frac{1}{2},k}^n \right) \\ & + \frac{\Delta t_s}{h_{x_3}} \left(\varphi_{i,j,k+\frac{1}{2}} u_{i,j,k+\frac{1}{2}}^n + \varphi_{i,j,k-\frac{1}{2}} u_{i,j,k-\frac{1}{2}}^n \right) - \\ & - \Delta t_s \varphi_{i,j,k} \mathbf{D} u_{i,j,k}^n, \end{aligned} \quad (2.27)$$

where $u_{i\pm\frac{1}{2},j,k}^n$, $u_{i,j\pm\frac{1}{2},k}^n$, $u_{i,j,k\pm\frac{1}{2}}^n$ denote the normal fluxes $\mathbf{u}^n \cdot \hat{\mathbf{n}}$ at the cells interfaces, and $\varphi_{i\pm\frac{1}{2},j,k}$, $\varphi_{i,j\pm\frac{1}{2},k}$, $\varphi_{i,j,k\pm\frac{1}{2}}$ are upwind approximations of $\varphi(S)$:

$$\varphi_{i\pm\frac{1}{2},j,k} = \begin{cases} \varphi(\mathbf{S}_{i,j,k}^n) & \text{if } u_{i\pm\frac{1}{2},j,k} \geq 0 \\ \varphi(\mathbf{S}_{i\pm 1,j,k}^n) & \text{otherwise} \end{cases}, \quad (2.28)$$

with analogous definitions for $\varphi_{i,j\pm\frac{1}{2},k}$ and $\varphi_{i,j,k\pm\frac{1}{2}}$. The term $(\Delta t_s \varphi_{i,j,k} \mathbf{D}u_{i,j,k}^n)$, with

$$\mathbf{D}u_{i,j,k}^n = u_{i+1,j,k}^n + u_{i-1,j,k}^n + u_{i,j+1,k}^n + u_{i,j-1,k}^n + u_{i,j,k+1}^n + u_{i,j,k-1}^n,$$

is added to compensate the small numerical divergence introduced by the Darcy's solver, an issue that is particularly important when using iterative methods to obtain the solution. This way, we assure the monotonicity of the numerical scheme. Let us introduce a second time step Δt_p and a parameter $C \in \{1, 2, \dots\}$ (the skipping constant) such that $\Delta t_p \equiv C \Delta t_s$ along a simulation. As shown in [26], instead of solving for the fluxes \mathbf{u} at each time step t^n , one can freeze the field \mathbf{u} and update it only every C fine time steps (with the new saturation field $\mathbf{S}(t^n + \Delta t_p)$), thus reducing the computational cost of a given simulation while maintaining good accuracy. More details on this methodology are given below along with an overview of our implementation.

2.3 Implementation aspects

The implemented code has two main components: 1) The Darcy (elliptic) solver and 2) The transport (hyperbolic) solver. A general pseudo code is shown in Algorithm 1. The Darcy solvers correspond to the implementation of the numerical methods presented in Section 2.1. For both implementations the Portable, Extensible Toolkit for Scientific Computation (PETSc)¹, version 3.13.0, was used as interface with HPC libraries to solve and precondition the related linear problems.

Input: \mathbf{S}^0 (initial saturation), C (skipping constant), Δt_s , T , *solver_type*

begin

| *Loop over time steps*

$t = 0$

$n_s = 0$, $n_p = 0$

while ($t \leq T$) **do**

| *Elliptic solver*

if ($\text{mod}(n_s, C) == 0$) **then**

$\mathbf{u}_\ell^{n_p} = \text{DarcySolver}(\text{solver_type}, \mathbf{S}^{n_s}, \mathbf{K})$

$n_p = n_p + 1$

end

| *Hyperbolic (fine grid) solver*

$\mathbf{S}^{n_s+1} = \text{TransportSolver}(\mathbf{S}^{n_s}, \mathbf{u}_\ell^{n_p})$

$t = t + \Delta t_s$

$n_s = n_s + 1$

$\mathbf{S}^{n_s} = \mathbf{S}^{n_s+1}$

end

end

Algorithm 1: General overview of the in-house developed code used in this work. The variable *solver_type* can be set to the Fine grid or the Multiscale solver.

2.3.1 Implementation details for the global fine grid solver

A key point in this work is to use an efficient fine grid global solver in order to make a fair comparison with the proposed multiscale solver. To that end, the linear problem (2.11) can be solved in parallel by using state-of-the-art linear algebra tools. In this work we choose the well known PETSc toolkit that allows to handle several combinations of linear solvers and preconditioners. Considering the sizes of the target problems we intend to consider (around 1 billion cells), three iterative linear solvers were tested, the Generalized Minimal Residual (GMRES), the Conjugate Gradient (CG) and the BiCGStab

¹<https://www.mcs.anl.gov/petsc>

(BCGSL) method. Two types of preconditioners were also considered, algebraic multigrid and incomplete factorization, being the former the only one that assured convergence and the best computational times. Among the algebraic multigrid methods available in PETSc, the best performance resulted from using either the “Multi Level Preconditioning Package” (ML) by Trilinos or the “BoomerAMG” implementation included in the library HYPRE² by the Lawrence Livermore National Laboratory³, both giving comparable results. However, up to its current version, ML was limited to 32-bits indices so it was not possible to use it in high resolution problems. By fixing the BoomerAMG as the preconditioner no relevant difference on computational times was observed when using GMRES, CG and or BCGSL. Hereafter, the results for the Fine Grid method will be relative to the GMRES solver preconditioned with BoomerAMG. The command line options used to set that configuration are shown in Table 1. The option `-ksp_rtol` sets the tolerance for the stopping criteria based on the relative preconditioned residual. Setting this option to `1e-8` was enough to observe convergence. An increase on this tolerance only provides small saving in computing time. To illustrate this we solve the SPE10 benchmark problem that have $\sim 1\text{M}$ unknowns distributed over 8 computational cores. Figure 2 shows the computational time spent by the Fine Grid solver and the resulting residual as a function of the number of GMRES iterations. A first eye catching conclusion is that the computational time slightly increases when the solution residual moves from 10^{-6} to 10^{-8} . It is also notable that the first iteration of GMRES takes most part of the time, which is related to the cost of computing the BoomerAMG operator. Similar conclusions apply to larger problems.

<code>-ksp_type</code>	<code>-ksp_rtol</code>	<code>-pc_type</code>	<code>-pc_hypre_type</code>
gmres	1e-8	hypre	boomeramg

Table 1: PETSc options used to implement the Fine Grid Solver.

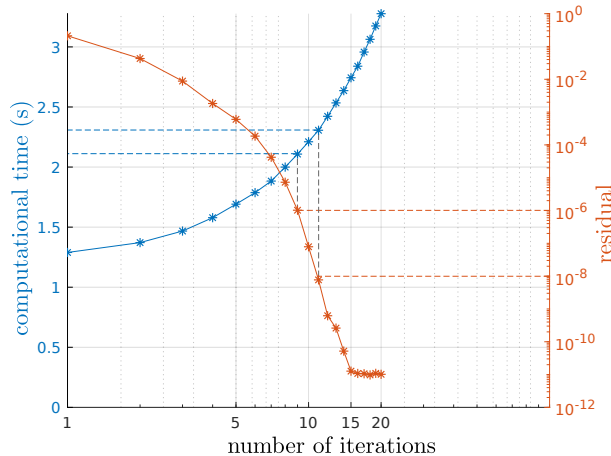


Figure 2: GMRES computational time and the solution residual as function of the number of iterations when preconditioning with BoomerAMG a 1M problem (SPE10 benchmark) with 8 computational cores.

To close this discussion, we remark that several of options are available through the PETSc interface to configure BoomerAMG. Preliminary tests were made by changing: the type of the multigrid cycle (V or W type), the number of cycles per GMRES iteration, the type of smoother to be applied on each grid, the type of interpolator and the use of nodal systems coarsening [27]. Each one of these options has a default setting that can be accessed by including the argument `-help` in the command line. In our experience changing these default parameters did not affect the solver’s efficiency significantly, so they are the ones adopted in our studies reported in Section 3.

²<https://computing.llnl.gov/projects/hypre-scalable-linear-solvers-multigrid-methods>

³<https://trilinos.github.io>

2.3.2 Implementation details of the Multiscale elliptic solver

Given a domain decomposition, the number of subdomains can be equal to or greater than the number of cores allocated for the MPI call (`mpirun -np`). An example of a distribution of subdomains is shown in Fig. 3. A constant number of subdomains is distributed to each MPI process, and hyper-threading is avoided forcing each one of these processes to run on a single physical core. A pseudo-code of the implementation is presented in Algorithm 2. Note that it is composed of three *loops*, all ranging over the subdomain decomposition, namely, 1) Local problems defining the MBFs are solved, 2) Interface problem is assembled and solved; 3) Multiscale solution is recovered. Between the first two loops the interface problem is solved and so MPI communications between processors are necessary. Note also that in order to obtain the multiscale solution, these two are the sole lines where communications are executed. In the postprocessing step MPI calls may also be involved. Computational time profiles for each stage of the implementation are reported in Section 3 for both MRCM and fine grid solvers.

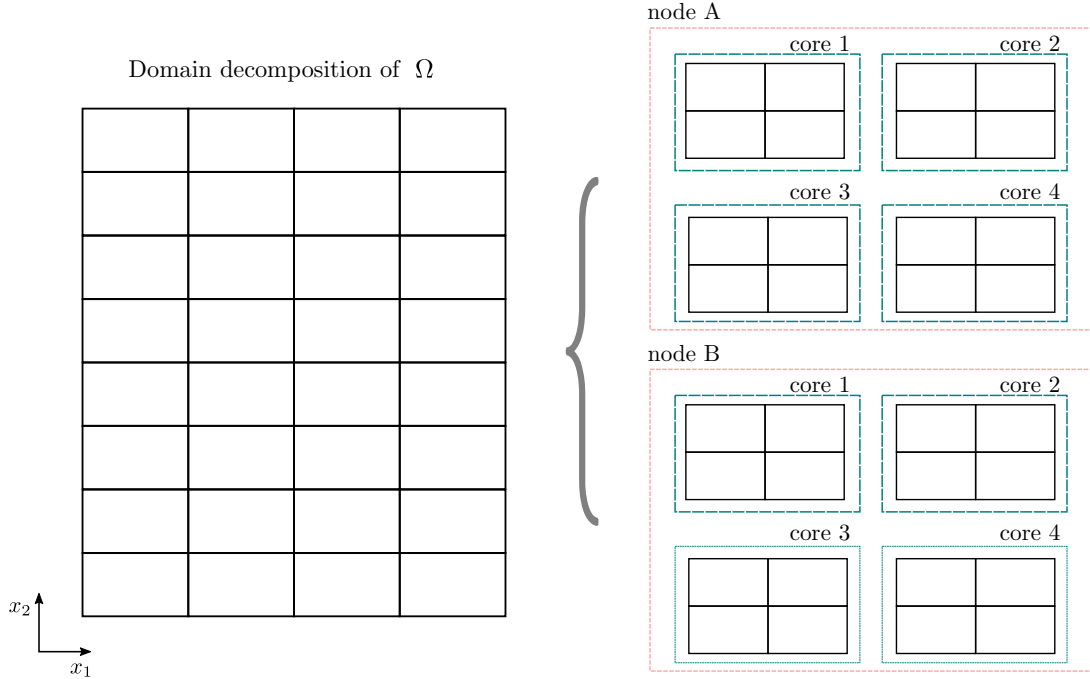


Figure 3: Example of a distribution for a decomposition of Ω into $4 \times 8 = 32$ subdomains. The MPI processes are evenly spread across a cluster of 2 nodes, with 4 physical cores per node, which results in an assignment of 4 subdomains per core.

```

Input:  $\tilde{\mathbf{K}} = \mathbf{K}$ , processor index  $r$ 
begin
  | Compute MBFs
  for  $\ell \in \mathcal{S}^r$  do
    Assembly  $\mathcal{A}_\ell^H$ ,  $\mathbf{f}_{\ell;\gamma}^H$ , and  $\mathbf{f}_{\ell,k;P}^H, \mathbf{f}_{\ell,k;U}^H$  for each  $k \in \mathcal{I}^\ell$ 
     $[\hat{\mathbf{p}}_{\ell,k;P}, \hat{\mathbf{p}}_{\ell,k;U}, \bar{\mathbf{p}}_{\ell;\gamma}] = \mathbf{LocalSolver}(\mathcal{A}_\ell^H, \mathbf{f}_{\ell,k;P}^H, \mathbf{f}_{\ell,k;U}^H, \mathbf{f}_{\ell;\gamma}^H)$ 
  end

  | Interface problem
   $\mathcal{A}^{\text{int}}, \mathbf{b}^{\text{int}} = \mathbf{Assembly}(\hat{\mathbf{p}}_{\ell,k;P}, \hat{\mathbf{p}}_{\ell,k;U}, \bar{\mathbf{p}}_{\ell;\gamma})$ 
   $X = \mathbf{InterfaceSolver}(\mathcal{A}^{\text{int}}, \mathbf{b}^{\text{int}})$ 

  | Recover Multiscale solution
  for  $\ell \in \mathcal{S}^r$  do
     $[p_\ell, \mathbf{u}_\ell] = \mathbf{ReconstructMscSolution}(\mathcal{A}_\ell^H, \hat{\mathbf{p}}_{\ell,k;P}, \hat{\mathbf{p}}_{\ell,k;U}, \bar{\mathbf{p}}_{\ell;\gamma}, X)$ 
  end

end

```

Algorithm 2: Pseudocode for the DD Multiscale mixed method.

| MBFs: $\mathbf{LocalSolver}()$

Let us now turn the attention to the computation of the MBFs. Consider a subdomain Ω_ℓ . The computations of the MBFs and the particular problem require solving several linear systems with the same underlying matrix \mathcal{A}_ℓ^H . Linear solvers based on matrix factorization are adequate for handling multiple right-hand-sides for the typical sizes of \mathcal{A}_ℓ^H , as anticipated. To support this choice, let us compare the computational times obtained when solving a Darcy problem by performing a LDL^\top factorization versus the computational cost corresponding to a GMRES solver with the Algebraic-Multigrid (AMG) preconditioning [28]. For these numerical experiments a discrete domain consisting of 45M cells is decomposed into 128, 256, 512, 1024, and 2048 subdomains, such that the number of cells of each Ω_ℓ ranges from 352K to 22K. Also, setting the ratio H/\bar{H} to 1 and 2 (H -refinement in one direction), the number of right-hand-sides (**nrhs**) ends up being 13 and 25, respectively. The computational times measured when distributing the subdomains along 32 cores are reported in Table 2. One observes that, even when the number of subdomains per core is increasing, a reduction of the number of cells on each Ω_ℓ results in smaller computational times irrespective of the solver.

#subdomains per core [total]	4 [128]	8 [256]	16 [512]	32 [1024]	64 [2048]
N_{Ω_ℓ}	352K	176K	88K	44K	22K
LDL $^\top$ factorization (nrhs = 13)	73.3	36.6	20.8	19.1	14.2
GMRES + AMG (nrhs = 13)	55.3	35.4	26.2	24.8	22.1
LDL $^\top$ factorization (nrhs = 25)	74.8	37.9	21.6	20.0	14.7
GMRES + AMG (nrhs = 25)	77.9	53.5	41.1	39.4	35.8

Table 2: Computing times (in seconds) for solving linear problems ($\mathcal{A}_\ell^H x = B$) with multiple right hand sides with two different solvers: a direct solver based on LDL^\top factorization, and an iterative GMRES preconditioned with an Algebraic Multigrid (AMG) method. The number of right-hand-sides is denoted by **nrhs**.

At this point, we may ask whether it is convenient or not to continue decreasing N_{Ω_ℓ} . Assuming the computational cost for solving the MBFs for a single subdomain is of order $N_{\Omega_\ell}^p$, a simple computation shows that for solving all the subdomains there is an advantage only if $p > 1$. We experimentally find p in Figure 4 that reports the computational times obtained by means of the MUMPS library [29, 30] when solving a 3-dimensional Laplacian along with thirteen right-hand-sides. For the MBFs computations, the best results are obtained by using the **amd** ordering scheme available in MUMPS. One can notice that p varies smoothly from $p \approx 1$ to $p \approx 2$. Hence, if all the problems are solve sequentially by one core,

there will exist a certain lower bound N_{Ω_ℓ} (typically around $\sim 20K$ for the problems of interest). Below this number the computational time associated to the local problems (MBFs) will approach a plateau. On the other hand, moving to very large subdomains would eventually lead to excessive computational times. This observation will be critical later on in selecting domain decompositions that balance the cost of the MBFs computations and the cost of the interface coupling problem. This will be explained next.

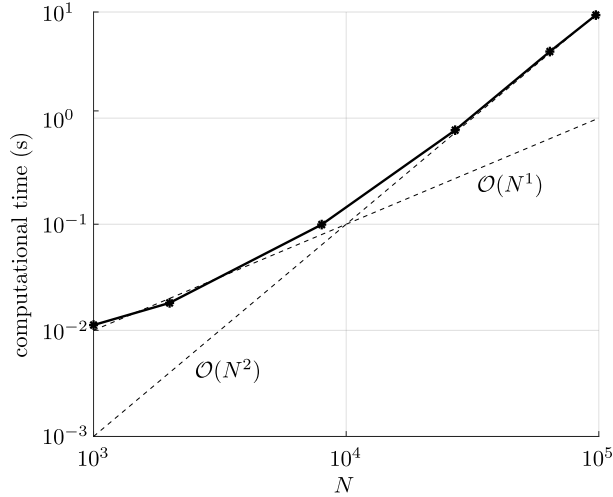


Figure 4: Computational times versus the system order (N) for solving thirteen linear problems along LDL^T factorization via MUMPS.

| Coupling problem: InterfaceSolver()

Based on results of the previous subsection, for billion cell reservoirs typical sizes of the interface system (2.18) to be solved ranges between several thousand up to less than a million unknowns. Hence, the computational burden of the interface resolution could be high as compared to the MBFs computations and the choice of the linear solver is critical for the computational efficiency. The best option we have found is the direct method based on LU factorization implemented in MUMPS using the `pard` ordering scheme. To illustrate this, the computational times of LU factorization for two different configurations of the MRCM for the same Darcy problem, the first one resulting in 431K unknowns and the second in 722K unknowns, are shown in Table 3. These configurations are later on used in Section 3.2.1. On the other hand, the GMRES preconditioned with the Additive Schwarz, incomplete LU factorization and Algebraic Multigrid methods were also tested, but none of these have provide smaller times than LU factorization. By means of a user-defined MPI communicator available in PETSc, one has the flexibility to choose over which MPI processes the resolution of the interface problem is distributed. In Table 3 the computational times corresponding to using 1 physical core (the root rank), half the computational capacity of a node, a whole node, and two computational nodes are reported. One observes that increasing the number of nodes beyond a single one does not provide significant speed-up for the 431K case whereas for the 722K case some non-negligible speed-up is attained. Based on these results from now on we adopt a direct method for the solution of the interface system distributed on a single node. Although not reported here for the sake of brevity, for smaller systems similar conclusions apply.

N_Γ	1 core	10 cores (half node)	20 cores (full node)	40 cores (two nodes)
431K	55.2	13.5	10.7	10.3
722K	155.7	35.1	26.0	22.3

Table 3: Computational times (in seconds) when the interface system is distributed on different number of cores.

To fully assess the performance of the MUMPS library for the problems of interest in this article, we solve the interface linear system arising from several settings to be used later on in the HPC results section. Figure 5 shows the time spent by the library to solve problems of varying sizes N_Γ from 5.5K

up to 724K interface unknowns. This study reveals that above $\sim 200\text{K}$ unknowns the behavior of the interface solver changes from linear to quadratic in N_Γ . Above such size, these results preclude the use of direct methods for solving the interface coupling system as is indeed verified in the experiments to be shown below.

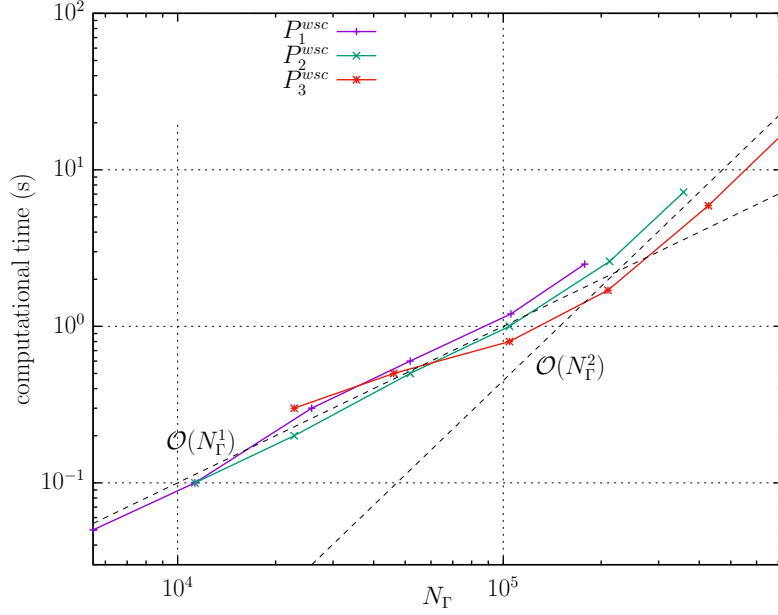


Figure 5: Computational times versus the system order (N_Γ) for solving typical interface linear problems using *LU* factorization via MUMPS. P_1^{wsc} , P_2^{wsc} and P_3^{wsc} refers to the weak scaling problems defined in Section 3.2.1.

3 HPC results

The results reported in this work were obtained in the *Euler Supercomputer*⁴, that is located at the Institute of Mathematical and Computer Science (ICMC) of the University of São Paulo at São Carlos⁵. The hardware specifications of listed in Table 4.

<i>Hardware specifications</i>	
Socket model	Intel Xeon E5-2680v2
Clock frequency	2.8 GHz
Cores per socket	10
Sockets per node	2
RAM per node	128 Gbytes
Communications	InfiniBand

Table 4: Specifications of the computational nodes where the implementations were tested.

3.1 Numerical setup

The numerical experiments are performed on a 5-spot geometry posed on a parallelepiped region $\Omega = [0, 1200] \times [0, 2200] \times [0, 120]$ (ft) with absolute permeability \mathbf{K} taken as the diagonal tensor provided by the SPE10 project [21] posed on a reference grid of $60 \times 220 \times 60$. Instead of considering the whole set of layers, for convenience in the design of the numerical experiments, only layers 26 to 85 have been selected in the x_3 direction. This field provides very heterogeneous channelized structures with high permeability

⁴<https://sites.google.com/site/clustercemai>

⁵<https://www.icmc.usp.br>

contrast and is a standard benchmark for numerical simulations in reservoir engineering. In order to conduct numerical experiments on finer grids than the original $60 \times 220 \times 60$, an L^2 projection of the reference permeability is performed to populate the tensor \mathbf{K} . Five vertical well columns modeled as volumetric sources/sinks, corresponding to the right hand side f in (2.4), with dimensions $20 \times 10 \times 120$ (ft) are distributed in the physical domain as follows: one central well Ω_w^0 injects water (this is $S_w(\mathbf{x}, t) = 1$, for $\mathbf{x} \in \Omega_w^0, t \geq 0$) such that one pore volume is injected (PVI) every five years and four oil producer wells $\Omega_w^i, i = 1, 2, 3, 4$ located at the corners of the domain as shown in Fig 6. No-flow boundary conditions are imposed on the external walls and the initial condition is set to $S_w(\mathbf{x}, 0) = 0$ on $\Omega \setminus \Omega_w^0$.

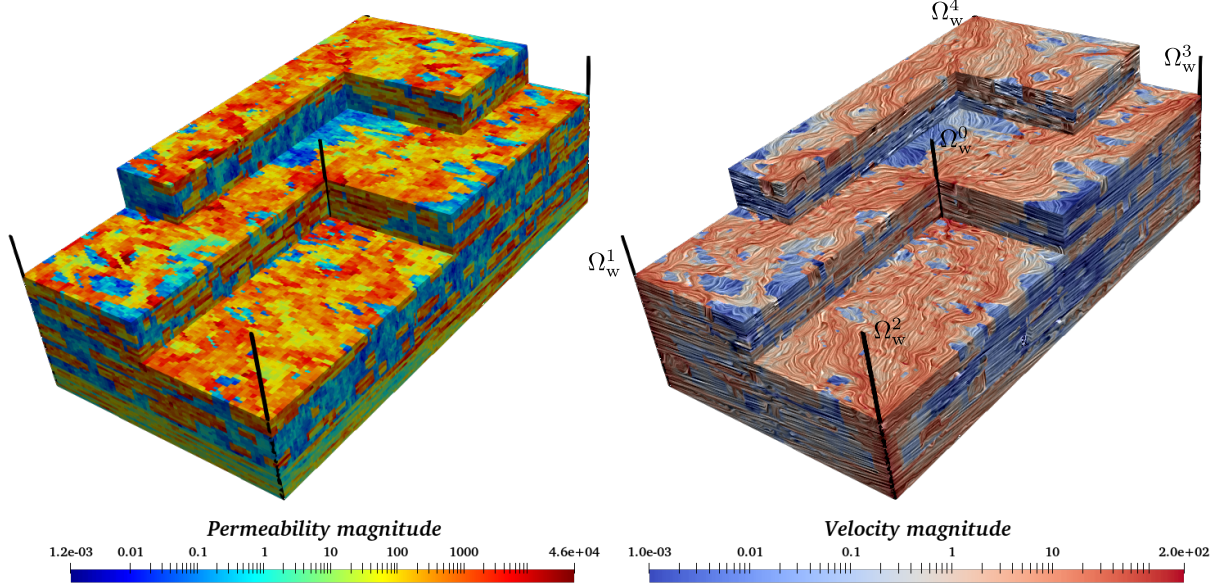


Figure 6: Permeability (magnitude) field \mathbf{K} cuts and wells disposition (left). Resulting flux magnitude for the MRCM (right).

As for the MRCM, the interface spaces \mathcal{P}_H and \mathcal{U}_H are spanned by constant functions defined over the domain decomposition with support on $\bar{H}_w \times \bar{H}_{\bar{w}}, w, \bar{w} = x_1, x_2, x_3$. One can check [5, 17, 18] for alternative choices of interface spaces. In line with previous works, the Robin condition parameter is defined locally over the interface grid as

$$\beta_l(\mathbf{x}) = \frac{\alpha H_l}{K_l(\mathbf{x})}, \quad (3.1)$$

where α is an algorithmic parameter, that unless otherwise mentioned, is set to 1.0, $H_l = \hat{\mathbf{n}}^\top \cdot [H_{x_1} \ H_{x_2} \ H_{x_3}]^\top$ and $K_l(\mathbf{x}) = \hat{\mathbf{n}}^\top \cdot \mathbf{K}(\mathbf{x}) \cdot \hat{\mathbf{n}}$.

Accuracy of the multiscale solutions is assessed by comparing them against the fine grid solution in terms of relative errors measured in the standard L^2 -norm for pressure and the weighted L^2 -norm given by $\|\mathbf{v}\|_{K^{-1}, \omega} = \left(\int_\omega K^{-1} |\mathbf{v}|^2 \right)^{\frac{1}{2}}$ for velocity.

3.2 Darcy solver: Weak and strong scaling

3.2.1 Weak scaling

The weak scaling properties of the algorithms is assessed in three different problem configurations as indicated in Table 5. The number of cores is increased as the fine grid is refined in the same proportion, so perfect weak scalability would imply the computational time to remain constant. The processor decomposition indicates the number of MPI processes and the core decomposition refers to the number of subdomains solved per core. The global number of unknowns for each case and the size of the local problems are also indicated in the table.

The average computational times of the different stages are reported in Table 6. In this table we show the total times for both fine grid and multiscale solver (MRCM), the time spent in MBFs computation and for the interface linear system solution. These times are obtained over several simulations such

core decomp.		4×2×4	8×2×4	8×2×8
# cores	processor decomp.	P_1^{wsc}	P_2^{wsc}	P_3^{wsc}
32	2×4×4	80×1760×160(22.5M)	160×1760×160(45M)	160×1760×320(90M)
64	4×4×4	160×1760×160(45M)	320×1760×160(90M)	320×1760×320(180M)
144	6×4×6	240×1760×240(101M)	480×1760×240(203M)	480×1760×480(406M)
288	6×4×12	240×1760×480(203M)	480×1760×480(406M)	480×1760×960(811M)
576	8×6×12	320×2640×480(406M)	640×2640×480(811M)	640×2640×960(1620M)
960	8×10×12	320×4400×480(676M)	640×4400×480(1350M)	640×4400×960(2700M)

Table 5: Domain decomposition and global grid for three problems for a weak scaling analysis.

	#cores	Fine	MRCM	MBFs	Int.	$\ e_p\ _{L^2(\Omega)}$	$\ e_v\ _{K^{-1},\Omega}$	N_Ω	N_Γ
P_1^{wsc}		$\frac{\sigma}{\mu} = 0.33$	$\frac{\sigma}{\mu} = 0.14$	$\frac{\sigma}{\mu} = 0.03$					
	32	14.4	7.2	6.7	0.0	0.45	0.38	22.5M	5.5K
	64	17.3	7.1	6.5	0.1	0.63	0.50	45.1M	11.3K
	144	22.0	7.4	6.6	0.3	0.60	0.54	101M	25.8K
	288	27.4	7.9	6.8	0.6	0.54	0.54	203M	51.8K
	576	28.6	8.9	7.0	1.2	0.51	0.53	406M	105.6K
	960	38.9	10.2	7.1	2.5	0.37	0.50	676M	178.0K
P_2^{wsc}		$\frac{\sigma}{\mu} = 0.25$	$\frac{\sigma}{\mu} = 0.18$	$\frac{\sigma}{\mu} = 0.03$					
	32	35.9	14.2	13.0	0.1	0.20	0.44	45.1M	11.3K
	64	50.4	14.1	12.9	0.2	0.74	0.57	90.1M	22.8K
	144	67.0	14.6	13.0	0.5	0.77	0.63	203M	51.8K
	288	83.3	15.6	13.4	1.0	0.73	0.63	406M	104.5K
	576	73.3	17.7	13.8	2.6	0.70	0.65	811M	212.3K
	960	68.9	22.6	14.1	7.2	0.57	0.62	1350M	358.0K
P_3^{wsc}		$\frac{\sigma}{\mu} = 0.27$	$\frac{\sigma}{\mu} = 0.21$	$\frac{\sigma}{\mu} = 0.03$					
	32	82.1	28.1	25.6	0.3	0.50	0.43	90.1M	22.8K
	64	112.2	27.8	25.4	0.5	0.67	0.56	180M	46.1K
	144	168.5	28.6	25.5	0.8	0.73	0.63	406M	104.5K
	288	196.7	30.5	26.4	1.7	0.72	0.63	811M	209.7K
	576	179.7	35.8	27.1	5.9	0.69	0.65	1620M	426.6K
	960	168.7	47.1	27.6	16.8	1.07	0.61	2700M	718.6K

Table 6: Computational times for the fine grid solver, the MRCM, the time to build the MBFs and the time for the interface solver as well the relative error for pressure and velocity.

that deviations from the mean are negligible. The relative pressure and velocity errors $\|e_p\|_{L^2(\Omega)}$ and $\|e_v\|_{K^{-1},\Omega}$ are also reported.

As one can notice the multiscale method has a better behavior with respect to weak scalability when compared to the fine grid solver. Computational times for both methods increase with the number of cores. The weak scalability with more than 288 cores for the MRCM declines. From Table 6 we also conclude that the total time taken by the MRCM is mainly dominated by the MBFs computation and the interface solver. As a measure of scalability performance, we report for each case the quantity σ/μ , which represents the relative deviation from the mean time along the scalability test. On one hand, the MBFs computation exhibits excellent weak scalability, an expected behavior as the number of local unknowns remains constant in each core. On the other hand, the interface resolution exhibits an inferior weak scalability behavior as the size of the linear system increases with the number of subdomains to be coupled in the multiscale process. This is explained by looking at the interface computing times. We observe a linear behavior with respect to N_Γ for $N_\Gamma \lesssim 200K$ and a transition to quadratic behavior from that point as previously shown in section 2.3.2. This has a deleterious effect for runs above $\sim 800M$. One should also notice that for the three problems in Table 6 the subdomains have the same 22K unknowns, but the cores handle twice the number of subdomains for P_j^{wsc} when compared to P_{j-1}^{wsc} .

Next, we take problem P_2^{wsc} and test two additional Darcy decompositions per processor, namely, $8 \times 1 \times 4$ and $8 \times 4 \times 4$ that lead to local Darcy problems of 44K and 11K unknowns, besides the original

setting of $8 \times 2 \times 4$ of 22K. Table 7 shows the total time for the fine grid, MRCM and time spent in the MBFs and interface solver phases. Note that the MBFs computations is around 14 seconds, since for these sizes of local problems, we have not entered into the quadratic behavior observed in Figure 4. Taking larger subdomains ($\gtrsim 44K$) implies in an increased MBFs computing time. This was actually confirmed by additional experiments, not shown here for the sake of brevity. Moreover, the time for the interface solver gets worse with the increase in the number of subdomains, as expected.

P_2^{wsc}		$8 \times 1 \times 4$ (44K)			$8 \times 2 \times 4$ (22K)			$8 \times 4 \times 4$ (11K)		
#cores	Fine	MRCM	MBFs	Int.	MRCM	MBFs	Int.	MRCM	MBFs	Int.
32	35.9	15.2	14.0	0.0	14.2	13.0	0.1	13.9	12.6	0.3
64	50.4	15.2	13.8	0.1	14.1	12.9	0.2	14.0	12.5	0.5
144	67.0	15.4	14.0	0.2	14.6	13.0	0.5	15.1	12.7	1.3
288	83.3	16.4	14.7	0.4	15.6	13.4	1.0	16.9	13.0	2.8
576	73.3	17.5	15.1	0.9	17.7	13.8	2.6	25.3	13.3	10.7
960	68.9	18.9	15.5	1.8	22.6	14.1	7.2	40.8	13.6	26.0

Table 7: Computational times to build the MBFs and solve the interface system for different local core decomposition of problem P_2^{wsc} . In parenthesis we show the number of unknowns of each subdomain.

3.2.2 Strong scaling

For the strong scaling assessment we consider three different global problems and two coarse scale decompositions. For a given coarse decomposition, the number of interface unknowns N_Γ and the size of the local problems N_Ω are fixed. These are displayed in Table 8. Strong scaling results for the different cases are summarized in Table 9. First, the optimum linear time decay is never observed for the three problems under consideration, neither for the fine grid nor for the multiscale solver. Nonetheless, the situation is significantly better with the multiscale solver as the total computing time goes as $\sim n^{-0.5}$ for problem P_1^{ssc} and $\sim n^{-0.85}$ for problems P_2^{ssc} and P_3^{ssc} , n being the number of cores. For the fine grid solver the computing time goes as $n^{-0.3}$ for P_1^{ssc} and $n^{-0.6}$ for P_2^{ssc} and P_3^{ssc} .

Note that, for a given number of cores, if we compare P_j^{ssc} with P_{j-1}^{ssc} an advantage of the multiscale solver with respect to the fine grid is observed in terms of scalability. We remark that the first point of P_3^{ssc} was omitted because it did not even fit in memory.

When fixing the problem size P_j^{ssc} , there is also a clear improvement in computational time of the multiscale solver as indicated in the Msc-Gain column, that is the ratio of the fine grid to the multiscale total times. Notice that the time spent in the interface solver is fixed for each coarse decomposition. This time is given in Table 9. When the processor grid increases each core ends up handling fewer subdomains. Thereby, the local solver shows good strong scalability as indicated in the MBFs column. Interestingly, the Msc-Gain is around 5 irrespective of the problem for the first coarse scale decomposition. However, as the burden of the interface system relatively grows, as is the case for the second decomposition, the Msc-Gain behaves differently depending on the problem, with values that oscillates between 1.5 up to 5.7. These results suggest the use of configurations with a limited number of interface unknowns as well as the necessity for better interface linear solvers.

3.2.3 Computational time dependence on the permeability field contrast

coarse decomp		$60 \times 10 \times 50$	$60 \times 20 \times 50$
N_Γ		171.8K	349.6K
#subdomains		30K	60K
fine grid		N_{Ω^ℓ}	N_{Ω^ℓ}
P_1^{ssc}	$360 \times 660 \times 300$ (71M)	2.4K	1.2K
P_2^{ssc}	$720 \times 1320 \times 600$ (570M)	19.0K	9.5K
P_3^{ssc}	$660 \times 2420 \times 600$ (958M)	32.0K	16.0K

Table 8: Strong scaling setup for three grid configurations and two coarse decompositions.

	Int. time		1.7			7.2		
	#cores	Fine	MRCM	Msc-Gain	MBFs	MRCM	Msc-Gain	MBFs
P_1^{ssc}	150	20.7	5.8	3.6	4.0	11.6	1.8	4.0
	300	17.5	3.9	4.5	2.2	9.6	1.8	2.2
	600	14.4	2.8	5.1	1.2	8.5	1.7	1.1
	1000	12.7	2.5	5.1	0.7	8.1	1.6	0.7
P_2^{ssc}	150	253.5	41.9	6.0	38.9	46.0	5.5	35.8
	300	110.9	23.7	4.7	21.4	27.9	4.0	19.2
	600	58.1	13.0	4.5	10.9	17.9	3.2	9.9
	1000	41.8	8.7	4.8	6.7	13.9	3.0	6.2
P_3^{ssc}	150	-	63.1	-	58.7	70.1	-	60.6
	300	230.8	36.1	6.4	33.1	40.8	5.7	32.7
	600	97.8	19.7	5.0	17.0	24.5	4.0	16.8
	1000	68.2	12.9	5.3	10.6	18.1	3.8	10.4

Table 9: Strong scaling assessment for the configurations defined in Table 8.

As a further verification of the relative advantage of our multiscale method based on direct solvers with respect to a fine grid solver based on iterative methods we investigate the effect on the computational performance of the permeability contrast, which is a critical parameter in reservoir engineering. To that end, let us take a parameter $\theta > 0$ and define the permeability tensor \mathbf{K}_θ by modifying each component of \mathbf{K} according to

$$\mathbf{K}_\theta^{ij}(\mathbf{x}) := (\mathbf{K}^{ij}(\mathbf{x}))^\theta.$$

This way, the permeability contrast ($c = \mathbf{K}_{\max}/\mathbf{K}_{\min}$) is modified as $c \rightarrow c^\theta$.

The modified SPE10 field is then projected on a fine grid consisting of 90M cells as previously explained. Computational times are reported for different values of θ in Table 10. In order to simplify the analysis, the computational times correspond to fixing the number of GMRES iterations to 12 (by setting `-ksp_max_it 12` and `-ksp_rtol 1e-20`). This was sufficient for the relative residual to reach a predefined tolerance of 10^{-8} in all runs. Interestingly, for low values of the contrast, the computational time spent for the iterative solver preconditioned with BoomerAMG decreases as c is increased. However, for high values of c . Similar to the SPE10 original contrast of $\sim 10^7$ and beyond, the computational time is nearly constant. This is consistent with [28], the seminal work that introduced the algebraic multigrid on which BoomerAMG is based. According to [28] the computational complexity relies on two parameters: on one hand, σ^Ω , denoting the ratio of the total number of points on all grids to that on the fine grid that is referred to as the grid complexity and on the other hand, σ^A , denoting the ratio of the total number of nonzeros entries in all the matrices to that in the fine grid matrix, which is called the operator complexity. In Table 10 it is observed that σ^Ω is relatively constant for the tested configurations, while the variation of σ^A is in direct relation to that of the computational time. As a result, the Msc-Gain varies from 8.2 for low values of θ up to something close to 3.7 for high values of θ .

θ	Contrast	σ^Ω	σ^A	time	Msc-Gain
0.30	1.9×10^2	2.13	13.6	115.3	8.2
0.48	4.4×10^3	2.03	9.87	75.9	5.4
0.65	8.7×10^4	1.97	6.57	54.1	3.9
0.83	2.0×10^6	1.97	5.93	51.5	3.7
1.0	4.0×10^7	1.98	6.05	50.4	3.6
1.17	7.8×10^8	1.99	6.11	50.4	3.6
1.35	1.8×10^{10}	2.00	6.16	51.9	3.7

Table 10: Dependence between the computational time of GMRES preconditioned with BoomerAMG when varying the contrast of the SPE10 benchmark.

3.2.4 Choice of multiscale method

In this article we have chosen the MRCM as a prototypical formulation from which other multiscale methods can be obtained by varying the interface Robin condition parameter α in (3.1). If we consider the limit $\alpha \rightarrow 0_+$, the multiscale solution satisfies pointwise pressure continuity at the skeleton Γ of the domain decomposition. On the other hand, as $\alpha \rightarrow \infty$, the multiscale solution satisfies pointwise velocity continuity at Γ . The numerical experiments presented so far were obtained for $\alpha = 1$, a choice based on prior numerical experience, for which neither the pressure nor the velocity are continuous on Γ . The velocity field produced by the multiscale method for such case is depicted in the top part Fig. 7 jointly with the fine grid solution. The multiscale solution corresponding to the extreme values $\alpha = 10^{-6}$ and 10^{+6} are displayed in the bottom part. The multiscale solution corresponding to $\alpha = 1$ captures

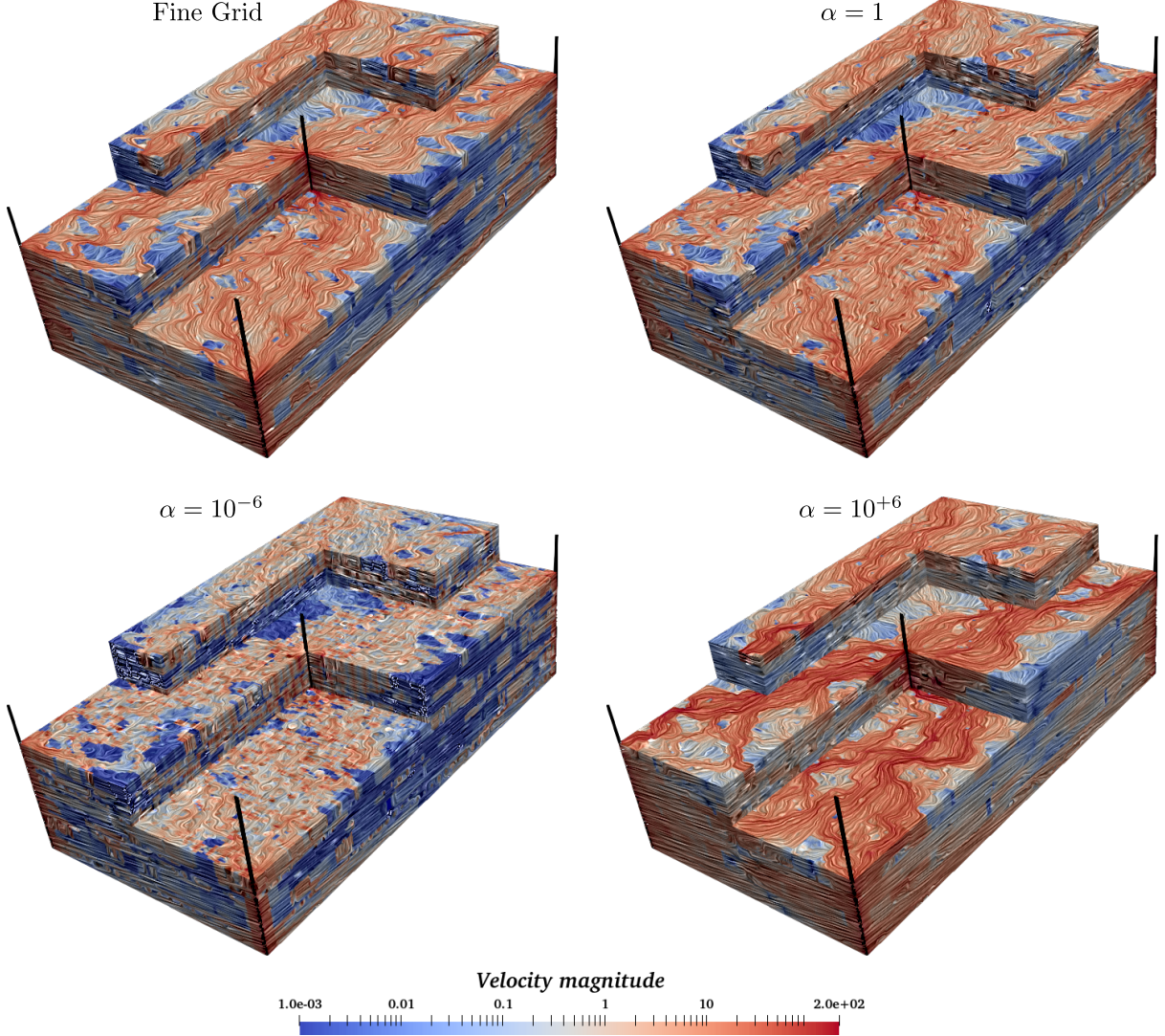


Figure 7: Fine grid solution and the multiscale solution for different choices of the α parameter .

remarkably well the underlying features of the permeability field showing great similarity to the fine grid solution. Numerical results for $\alpha = 10^{-6}$ and 10^{+6} are significantly far away from those. This is better noticed in in Figs. 8 and 9, in which the 3D solutions are intersected by planes corresponding to layers 36 and 85 of the SPE10, precisely where interesting highly channelized structures are located. The reference solution for layer 36 is displayed at the top of Fig. 8 followed by the multiscale solutions. The inserts show zoomed regions of interest, one for each choice of α , pared to the corresponding area in the reference solution to ease the comparison. For the MRCM(10^{+6}), the zoomed area displays a region having a high permeability channel and a low permeability background. We notice in such case the method does not detect the presence of the channel and the fluid passes through it. For the MRCM(10^{-6}) the zoomed area also points to a channel with high permeability. Whilst the channelized

structure is better represented, unphysical recirculation patterns are observed near the corners of the domain decomposition. Similar patterns are also observed in Fig. 9 that corresponds to layer 85. More sophisticated choices of the algorithmic parameter as those proposed in [12] can be adopted with the potential to deliver more accurate results at the same computational cost.

Also, accuracy can be improved by making smarter choices of the interface spaces defined over the skeleton Γ . We have limited so far to the piecewise constant case. In our implementation, nonetheless, we can easily perform an H -refinement over Γ as explained in 2.1.2. To illustrate this, Fig. 10 shows the solution for the MRCM(10^{-6}) obtained by halving the interface elements (i.e., $\bar{H} = H/2$). Although the dimension of the interface coupling system multiplies by 4, the computation of multiscale basis function comes almost at no cost, since it only involves the solution of a linear system for a greater number of right hand sides. One can notice an overall improvement of the solution especially in regions of high-speed magnitude as occurs close to wells (see the zoomed areas in the inserts).

Further improvements could make use of informed functions spaces or spaces based on physics (see [17, 18]) that can better capture the underlying variations of the rock formation, with possibly a reduced number of degrees of freedom.

3.2.5 Two-phase flow simulations

As a final numerical experiment we solve a two-phase flow problem by solving (2.2)-(2.6) (see Algorithm 1). Results are obtained for both the Multiscale mixed method and the Fine Grid solver. According to (2.15) the velocity solutions produced by the MRCM are conservative in a scale that corresponds to the support of the basis functions that span the pressure interface space \mathcal{P}_h . As the supports are usually chosen such that $\bar{H}_{x_j} \gg h_{x_j}$, the velocity solutions are in general discontinuous at the fine level h_{x_j} , except for very large values of the algorithmic parameter α . A postprocessing of the velocity field is necessary prior to solving the hyperbolic transport problem. Here the *Mean* method [20] has been chosen to that end for the sake of simplicity. A unique flux over Γ is defined based on the average value of the velocity on interfaces between adjacent subdomains. These fluxes are then used as Neumann boundary conditions to compute local problems on each Ω^ℓ . Given the multiscale solution \mathbf{u}_H , this amounts to computing the unique velocity

$$\bar{\mathbf{U}}_h^\Gamma \doteq \frac{1}{2} (\mathbf{u}_H^+|_\Gamma + \mathbf{u}_H^-|_\Gamma).$$

that in line with (2.15) transfers the same mass across the interfaces as the multiscale solution. For each subdomain Ω_i , we solve

$$\begin{cases} \tilde{\mathbf{u}}_h^i &= -K \nabla \tilde{p}_h^i & \text{in } \Omega_i, \\ \nabla \cdot \tilde{\mathbf{u}}_h^i &= f & \text{in } \Omega_i, \\ \tilde{\mathbf{u}}_h^i \cdot \tilde{\mathbf{n}}^i &= \mathbf{u}_H|_{\partial\Omega_i} \cdot \tilde{\mathbf{n}}^i & \text{on } \partial\Omega_i \cap \partial\Omega, \\ \tilde{\mathbf{u}}_h^i \cdot \tilde{\mathbf{n}}^i &= \bar{\mathbf{U}}_h^\Gamma|_{\partial\Omega_i} \cdot \tilde{\mathbf{n}} & \text{on } \partial\Omega_i \cap \Gamma, \end{cases} \quad (3.2)$$

that is conservative on the fine scale. The procedure involves communications to compute the unique flux. For it, a single `MPI_Allreduce` call is sufficient having a negligible cost in the overall computational time. However, the solution of the local problems (3.2) involves a new linear subdomain solve. Certainly, this is not the best method as reported in [20] where alternative computationally more efficient and accurate postprocessing methods can be found, although their implementation is a bit more involved and is left for future work.

The multiscale performance is assessed by comparing the production curves. We choose the computational setting adopted for the P_2^{wsc} distributed over 288 cores. The simulation is performed until $T_{PVI} = 0.2$, well beyond the breakthrough time for all production wells. The frequency of Darcy solves comes from a skipping constant $C = 600$. The time step Δt_s in (2.27) satisfies the CFL condition [31, 32], which translates to

$$\Delta t_s \leq \frac{\min \{h_{x_1}, h_{x_2}, h_{x_3}\}}{\max_{\Omega} |\varphi'(\mathbf{S}^n) \mathbf{u}^n|}. \quad (3.3)$$

The oil is being extracted from the four wells located at the corners of Ω . The production (\mathcal{P}_{oil}) and water-cut (W_i) curves correspond to the fraction of oil and water for each production well, $i = 1 \dots 4$ as a function of time. The $\mathcal{P}_{oil}(t)$ is computed according to

$$\mathcal{P}_{oil}(t) = \frac{\sum_{i=1}^4 \int_{\partial\Omega_w^i} (1 - \varphi(S_w(\mathbf{x}, t))) \mathbf{u}(\mathbf{x}, t) \cdot d\mathbf{\Gamma}}{\sum_{i=1}^4 \int_{\partial\Omega_w^i} \mathbf{u}(\mathbf{x}, t) \cdot d\mathbf{\Gamma}},$$

whereas for each production well ($i = 1 \dots 4$) one has

$$W_i(t) = \frac{\int_{\partial\Omega_w^i} \varphi(S_w(\mathbf{x}, t)) \mathbf{u}(\mathbf{x}, t) \cdot d\mathbf{\Gamma}}{\int_{\partial\Omega_w^i} \mathbf{u}(\mathbf{x}, t) \cdot d\mathbf{\Gamma}}.$$

The time variable used to present results is in $T_{\text{PVI}}(t)$ units defined as:

$$T_{\text{PVI}}(t) = \frac{1}{V_p} \int_0^t \int_{\Omega_w^0} f(\mathbf{x}, \tau) d\mathbf{x} d\tau,$$

being V_p the reservoir's total pore-volume and f the source term (2.4).

The computational times for the complete simulations are 473 hours for the Fine grid solver and 190 hours for the multiscale method. Since the number of Darcy calls differs from one case to the other due to adaptivity of Δt_s , comparison of total times is less meaningful. The computational time of one single call being a more representative figure. For the considered setting the cost of a single call for the elliptic solver when using the MRMC takes 29 seconds, whereas it takes 83 seconds for the fine grid solver. Recall that prior to solving the transport equation after each Darcy solve one needs to execute the velocity post-processing which as mentioned can be significantly reduced in the future by implementing more efficient techniques. To conclude, a comparison of the oil production curves resulting from the two-phase flow solver using the Fine Grid and the MRCM is shown in Figure 11. There is a good agreement of the multiscale solution to the fine grid one. The maximum difference in the oil fraction produced is around 6%, which takes place at $T_{\text{PVI}} = 0.07$, after which the difference decreases monotonically. By looking at the watercuts curves on each production well, plotted in Figure 12, most part of the error is concentrated at wells 2 and 1.

4 Conclusions and outlook

We have presented an HPC implementation for multiscale mixed methods based on non-overlapping domain decomposition techniques, especially tailored for the simulation of flow in porous media. We considered problems ranging from a several million up to a billion fine grid cells. The accuracy and computational performance of the scheme as well as its scalability properties have been assessed in problems involving anisotropic highly heterogeneous permeability fields based on the SPE10 benchmark. For testing of different multiscale options the general framework offered by the MRCM method have been adopted.

The main conclusions that emerge from exhaustive numerical experimentation are:

- The best computational times are obtained for the multiscale method by using direct solvers for both the local problems and the interface system. In the former case, this comes from the fact that several right hand sides must be solved for each subdomain. In the latter case, this comes from the conditioning of the coupling system.
- Assessment of the direct solver used in this work (MUMPS) shows that decreasing the number of local unknowns below a certain threshold $N_{\Omega^\ell} \sim 40\text{K}$, yielding more subdomains per processor, will eventually lead to a plateau in computing time of the MBFs, since the behavior changes from quadratic to linear in N_{Ω^ℓ} at this point.
- In general, the multiscale method exhibits better weak scalability and computational performance for the problem sizes considered in this work. This depends on the number of local and interface unknowns that can be chosen as the domain decomposition is specified. This good behavior is limited by the size of the interface system. For values of $N_\Gamma \gtrsim 200\text{K}$ a decline in scalability properties of the scheme is observed.
- The strong scalability assessment reveals that if the number of processors available is a limiting factor, the multiscale mixed method is an excellent asset, either because the problem may not fit in memory for the fine grid solver or due to the significant gain in computing time obtained, that can be as high as 6.
- One advantage of the strategy adopted is that it allows to estimate a priori the computing time of the solver irrespective of the problem and permeability contrast.

- Accuracy of the multiscale solver has been also assessed in a two phase flow scenario in a problem involving 406M unknowns. Results for the production curves and water cuts are promissory yielding errors smaller than 6% with respect to the fine grid solution.

Results presented so far show the potential of Multiscale Mixed Methods to solve large scale porous media problems.

Acknowledgments

The authors gratefully acknowledge the financial support received from the Brazilian oil company Petrobras grant 2015/00400-4, from the São Paulo Research Foundation FAPESP/CEPID/CeMEAI grant 2013/07375-0, and from Brazilian National Council for Scientific and Technological Development CNPq grants 305599/2017-8 and 310990/2019-0. This research was carried out using computational resources from the Cluster Euler, Centre for Mathematical Sciences Applied to Industry (CeMEAI).

References

- [1] A. M. Manea, J. Sewall, and H. A. Tchelepi. Parallel multiscale linear solver for highly detailed reservoir models. *SPE Journal*, 21(06):2062–2078, 2016.
- [2] L. J. Durlofsky, Y. Efendiev, and V. Ginting. An adaptive local–global multiscale finite volume element method for two-phase flow simulations. *Advances in Water Resources*, 30(3):576–588, 2007.
- [3] K.-A. Lie, O. Møyner, J. R. Natvig, A. Kozlova, K. Bratvedt, S. Watanabe, and Z. Li. Successful application of multiscale methods in a real reservoir simulator environment. *Computational Geosciences*, 21(5-6):981–998, 2017.
- [4] A. Francisco, V. Ginting, F. Pereira, and J. Rigelo. Design and implementation of a multiscale mixed method based on a nonoverlapping domain decomposition procedure. *Math. Comput. Simul.*, 99:125–138, 2014.
- [5] R. T. Guiraldello, R. F. Ausas, F. S. Sousa, F. Pereira, and G. C. Buscaglia. The multiscale Robin coupled method for flows in porous media. *Journal of Computational Physics*, 355:1–21, 2018.
- [6] T. Arbogast, G. Pencheva, M. F. Wheeler, and I. Yotov. A multiscale mortar mixed finite element method. *Multiscale Modeling & Simulation*, 6(1):319–346, 2007.
- [7] P. Jenny, S.H. Lee, and H.A. Tchelepi. Multi-scale finite-volume method for elliptic problems in subsurface flow simulation. *Journal of Computational Physics*, 187(1):47–67, 2003.
- [8] Yalchin Efendiev, Juan Galvis, and Thomas Y. Hou. Generalized multiscale finite element methods (gmsfem). *Journal of Computational Physics*, 251:116–135, 2013.
- [9] Thomas Y. Hou and Xiao-Hui Wu. A multiscale finite element method for elliptic problems in composite materials and porous media. *Journal of Computational Physics*, 134(1):169–189, 1997.
- [10] C. Harder, D. Paredes, and F. Valentin. A family of multiscale hybrid-mixed finite element methods for the darcy equation with rough coefficients. *Journal of Computational Physics*, 245:107–130, 2013.
- [11] V. Kippe, J. E. Aarnes, and K.-A. Lie. A comparison of multiscale methods for elliptic problems in porous media flow. *Computational Geosciences*, 12(3):377–398, 2008.
- [12] F. F. Rocha, F. S. Sousa, R. F. Ausas, G. C. Buscaglia, and F. Pereira. Multiscale mixed methods for two-phase flows in high-contrast porous media. *Journal of Computational Physics*, 409:109316, 2020.
- [13] Manea A. M., Sewall J., and Tchelepi H. A. Parallel multiscale linear solver for highly detailed reservoir models. *SPE Journal*, 21 (6):2062–2078., 2016.
- [14] A. M. Manea, Hajibeygi H., Vassilevski P., and H.A. Tchelepi. Parallel enriched algebraic multiscale solver. 2017, doi:10.2118/182694-MS.

- [15] Puscas M., Enchery G., and Desroziers S. Application of the mixed multiscale finite element method to parallel simulations of two-phase flows in porous media. *Oil & Gas Science and Technology*, 73, 2018.
- [16] E. Abreu, P. Ferraz, A. M. Espírito Santo, F. Pereira, L. G. C. Santos, and F. S. Sousa. Recursive formulation and parallel implementation of multiscale mixed methods, 2020.
- [17] R. T. Guiraldello, R. F. Ausas, F. S. Sousa, F. Pereira, and G. C. Buscaglia. Interface spaces for the multiscale robin coupled method in reservoir simulation. *Mathematics and Computers in Simulation*, 164:103 – 119, 2019.
- [18] F. F. Rocha. *Enhanced multiscale mixed methods for two-phase flows in high-contrast porous media*. PhD thesis, Instituto de Ciências Matemáticas e de Computação, USP, 2020.
- [19] Rocha F., Ausas F. S. Sousa, R. F., Pereira F., and Buscaglia G. C. Interface spaces based on physics for multiscale mixed methods applied to flows in fractured-like porous media, 2021.
- [20] R. T. Guiraldello, R. F. Ausas, F. S. Sousa, F. Pereira, and G. C. Buscaglia. Velocity postprocessing schemes for multiscale mixed methods applied to contaminant transport in subsurface flows. *Computational Geosciences*, 24(3):1141–1161, 2020.
- [21] M. Christie and M. J. Blunt. Tenth SPE comparative solution project: a comparison of upscaling techniques. 2001. SPE Reservoir Simulation Symposium 2001.
- [22] J. W. Sheldon and W. T. Cardwell. One-dimensional, incompressible, noncapillary, two-phase fluid flow in a porous medium. *Transactions of the AIME*, 216(01):290–296, 1959.
- [23] Uri M. Ascher, Steven J. Ruuth, and Brian T. R. Wetton. Implicit-explicit methods for time-dependent partial differential equations. *SIAM Journal on Numerical Analysis*, 32(3):797–823, 1995.
- [24] Zhangxin Chen, Guanren Huan, and Baoyan Li. An improved IMPES method for two-phase flow in porous media. *Transport in porous media*, 54(3):361–376, 2004.
- [25] Stevens Paz, Alfredo Jaramillo, Rafael T. Guiraldello, Roberto F. Ausas, Fabricio S. Sousa, Felipe Pereira, and Gustavo C. Buscaglia. An adaptive time stepping algorithm for impes with high order polynomial extrapolation. *Applied Mathematical Modelling*, 91:1100–1116, 2021.
- [26] Z. Chen, G. Huan, and B. Li. An improved impes method for two-phase flow in porous media. *Transport in porous media*, 54(3):361–376, 2004.
- [27] R. Falgout. Hypre user’s manual. <http://www.llnl.gov/CASC/hypre>, 2017. Accessed: 2020-11-30.
- [28] J. W. Ruge and K. Stüben. 4. Algebraic Multigrid. In *Multigrid Methods*, pages 73–130. Society for Industrial and Applied Mathematics, 1987.
- [29] P. R. Amestoy, I. S. Duff, J. Koster, and J.-Y. L’Excellent. A fully asynchronous multifrontal solver using distributed dynamic scheduling. *SIAM Journal on Matrix Analysis and Applications*, 23(1):15–41, 2001.
- [30] P. R. Amestoy, A. Guermouche, J.-Y. L’Excellent, and S. Pralet. Hybrid scheduling for the parallel solution of linear systems. *Parallel Computing*, 32(2):136–156, 2006.
- [31] Richard Courant, Kurt Friedrichs, and Hans Lewy. Über die partiellen differenzengleichungen der mathematischen physik. *Mathematische annalen*, 100(1):32–74, 1928.
- [32] Keith H Coats et al. A note on impes and some impes-based simulation models. *SPE Journal*, 5(03):245–251, 2000.

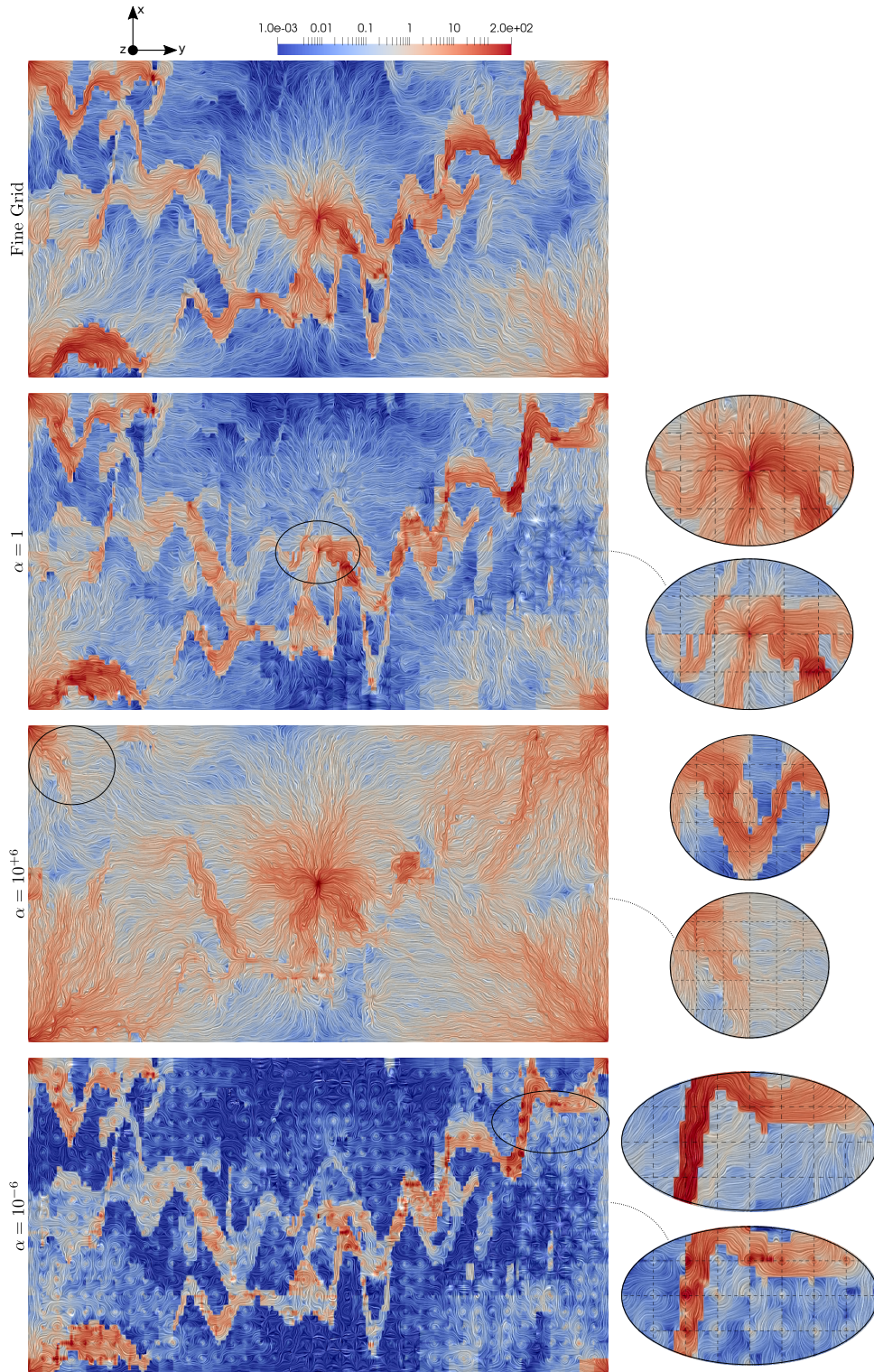


Figure 8: Fine grid solution and the multiscale solution for different choices of the α parameter for a cut in layer 36 in x_3 plane of the 3D solution.

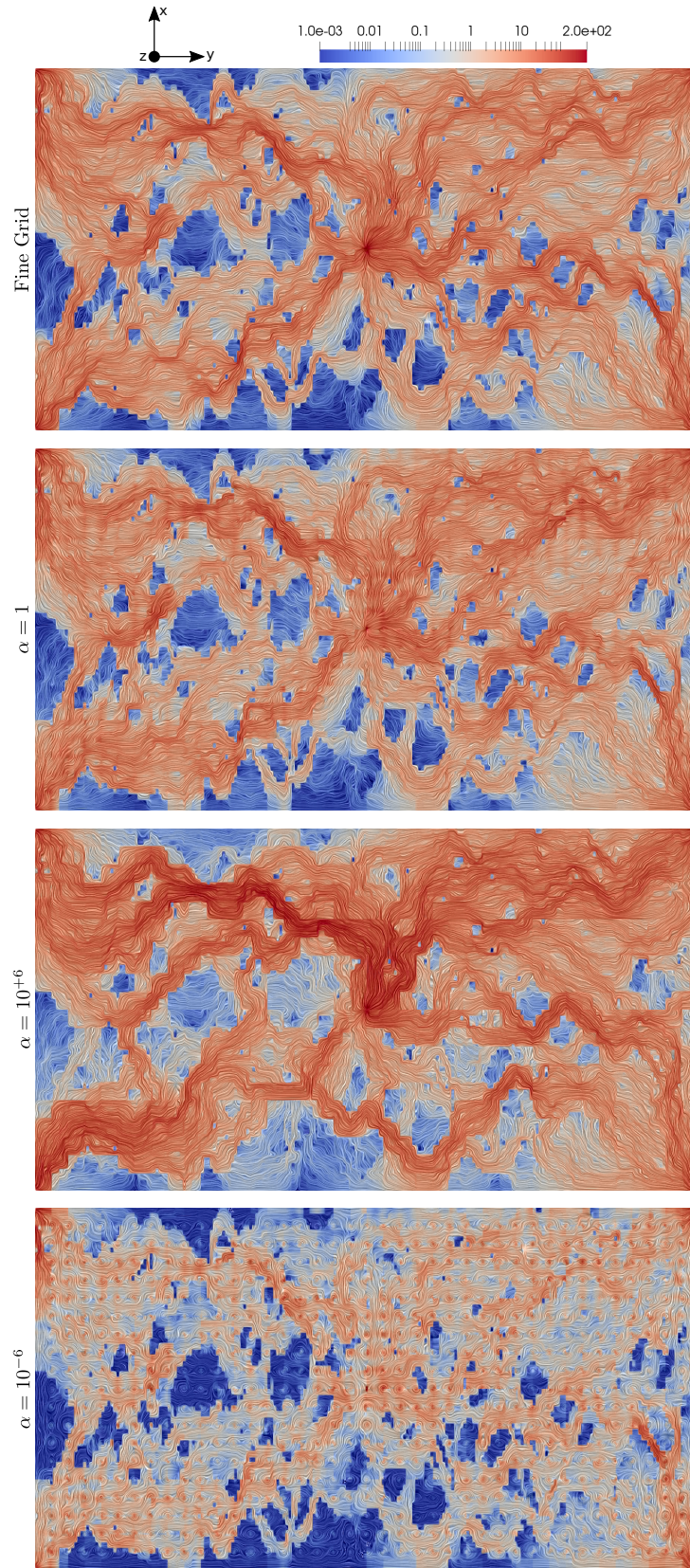


Figure 9: Fine grid solution and the multiscale solution for different choices of the α parameter for a cut in layer 85 in x_3 plane of the 3D solution.

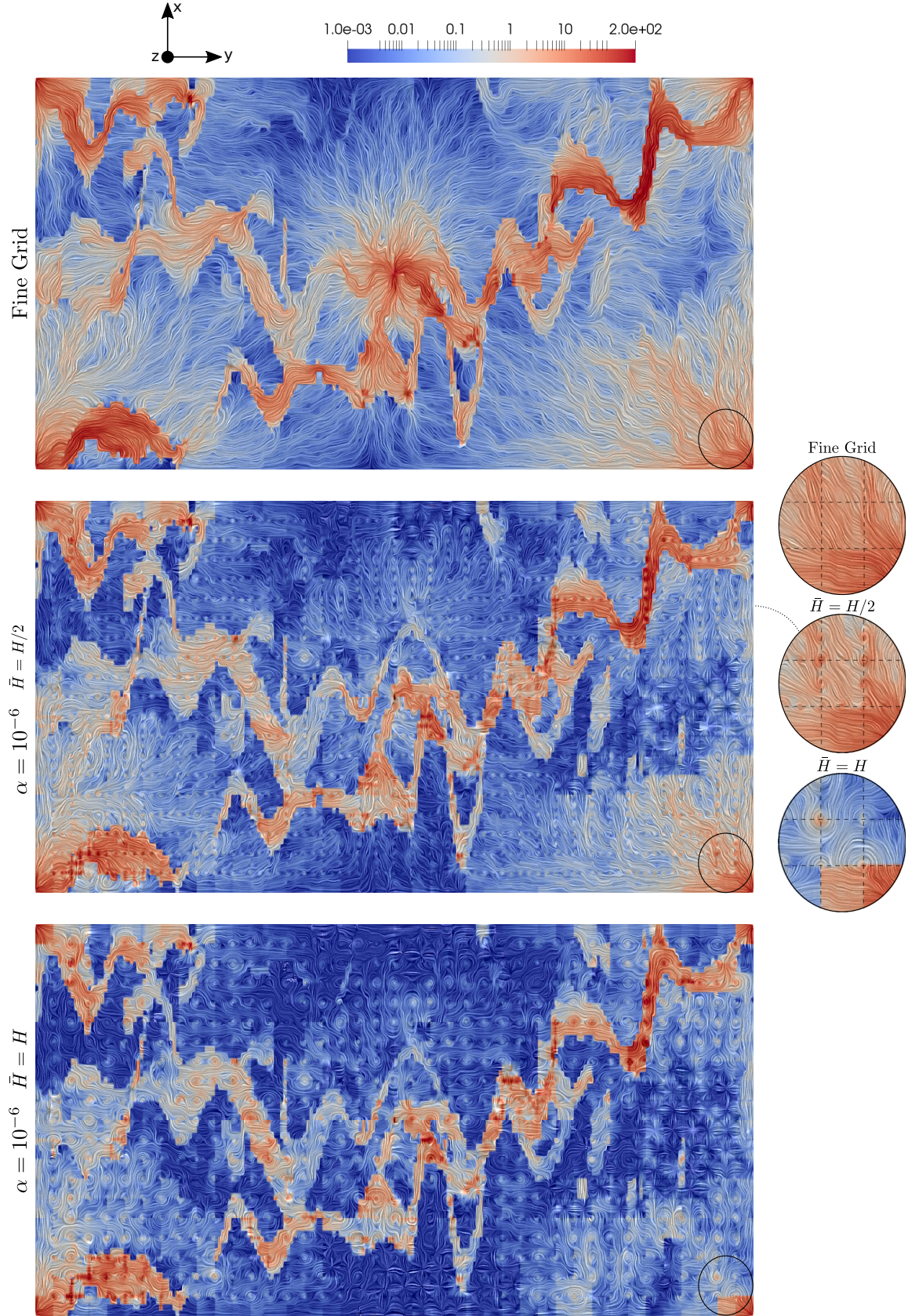


Figure 10: Fine grid solution and the multiscale solution for $\alpha = 10^{-6}$ and two values of \bar{H} for a cut in layer 36 along the x_3 plane of the 3D solution.

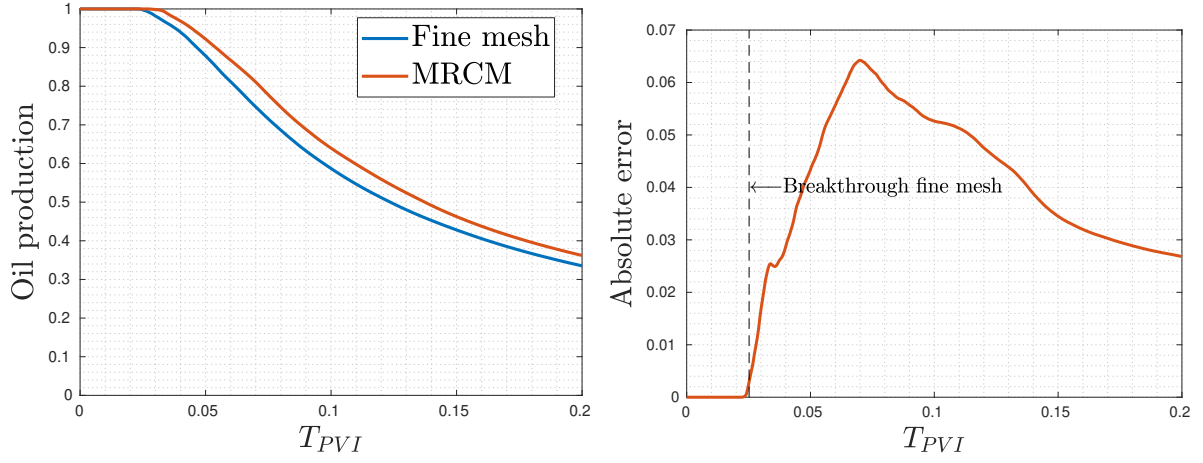


Figure 11: Oil production curve resulting when using fine mesh and MRCM for elliptic problems (left). Absolute error between these curves (right).

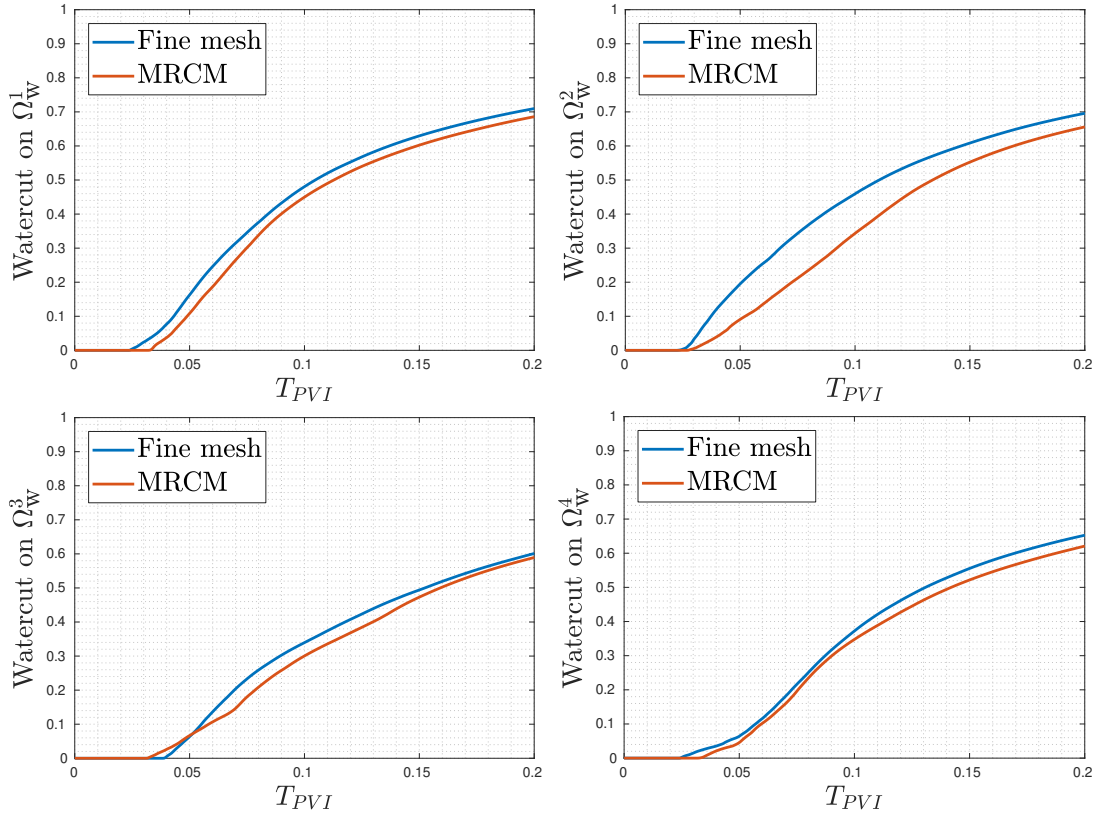


Figure 12: Watercut on wells Ω_w^i , $i = 1, 2, 3, 4$.